

DOCUMENT CONTROL SHEET

	ORIGINATOR'S REF. NLR TP 96047 U		SECURITY CLASS. Unclassified												
ORIGINATOR National Aerospace Laboratory NLR, Amsterdam, The Netherlands															
TITLE Failure and cracking of Inconel 718 air supply manifold support rods - A service-related contribution to IEPG TA 31 -															
PRESENTED AT															
AUTHORS R.J.H. Wanhill, J.A.M. Boogers, H.N. Huisman and H.H. Ottens		DATE 960122	pp    ref 87    17												
DESCRIPTORS <table style="width: 100%; border: none;"> <tr> <td style="width: 50%;">Bending fatigue</td> <td style="width: 50%;">Manifolds</td> </tr> <tr> <td>Cracking (fracturing)</td> <td>Metal surfaces</td> </tr> <tr> <td>Failure analysis</td> <td>Protective coatings</td> </tr> <tr> <td>Fractography</td> <td>Rods</td> </tr> <tr> <td>Inconel (trademark)</td> <td>Turbofan engines</td> </tr> <tr> <td>Intake systems</td> <td></td> </tr> </table>				Bending fatigue	Manifolds	Cracking (fracturing)	Metal surfaces	Failure analysis	Protective coatings	Fractography	Rods	Inconel (trademark)	Turbofan engines	Intake systems	
Bending fatigue	Manifolds														
Cracking (fracturing)	Metal surfaces														
Failure analysis	Protective coatings														
Fractography	Rods														
Inconel (trademark)	Turbofan engines														
Intake systems															
ABSTRACT In 1995 an air supply manifold support rod from a high-performance turbofan engine failed by bending fatigue. The rod material was Inconel 718, operating at about 550° in an air environment. Diagnostic aspects of the failure (fatigue in bending, Stage I and Stage II fatigue fracture characteristics, and interference colours due to fracture surface oxidation) were aided by test results from the European collaborative programme IEPG TA 31: Lifting Concepts for Military Aero-Engine Components. Bending of the rod was caused by relative movement of the inner and outer sections of a connection between the diffuser case air supply manifold, whereby accommodatory swivelling of a spherical ends of the rod in the spherical seatings of the connection was prevented by contact pressure, fretting and binding. A contributory factor is likely to have been decomposition of an anti-galling compound applied to the spherical contact surfaces. This decomposition, and hence loss of function, could have begun at temperatures well below the normal operating temperatures of the rod. Recommendations were made for the alternative anti-galling compounds or a plasma-sprayed coating, which is a less suitable option. It was also recommended to thoroughly inspect the rods in other engines, as an addition to the specified maintenance procedure. This additional inspection was well under way by the beginning of 1996.															

NLR TECHNICAL PUBLICATION

TP 96047 U

FAILURE AND CRACKING OF INCONEL 718 AIR SUPPLY  
MANIFOLD SUPPORT RODS

- A service-related contribution to IEPG TA 31 -

by

R.J.H. Wanhill, J.A.M. Boogers,

H.N. Huisman and H.H. Ottens

This investigation has been done partly under contract to the Netherlands Agency for Aerospace Programs (NIVR), contract no. 07002N, as part of the NLR's workshare in IEPG TA 31: Lifing Concepts for Military Aero-Engine Components.

Division : Structures and Materials

Prepared : RJHW/JAMBA/SHNH/KHO/H<sub>2</sub>O '2/3

Approved : RJHW/W

Completed : 960122

Order number : 101.398/543.902

Typ. : JS





## Summary

In 1995 an air supply manifold support rod from a high-performance turbofan engine failed by bending fatigue. The rod material was Inconel 718, operating at about 550 °C in an air environment. Diagnostic aspects of the failure (fatigue in bending, Stage I and Stage II fatigue fracture characteristics, and interference colours due to fracture surface oxidation) were aided by test results from the European collaborative programme IEPG TA 31: Lifting Concepts for Military Aero-Engine Components.

Bending of the rod was caused by relative movement of the inner and outer sections of a connection between the diffuser case air supply tube and the bleed air supply manifold, whereby accommodatory swivelling of the spherical ends of the rod in the spherical seatings of the connection was prevented by contact pressure, fretting and binding. A contributory factor is likely to have been decomposition of an anti-galling compound applied to the spherical contact surfaces. This decomposition, and hence loss of function, could have begun at temperatures well below the normal operating temperatures of the rod.

Recommendations were made for alternative anti-galling compounds or a plasma-sprayed coating, which is a less suitable option. It was also recommended to thoroughly inspect the rods in other engines, as an addition to the specified maintenance procedure. This additional inspection was well under way by the beginning of 1996.



## Contents

Nomenclature	6
<b>1 Introduction</b>	<b>7</b>
<b>2 Scope of the failure investigation</b>	<b>9</b>
<b>3 Fractography</b>	<b>11</b>
3.1 Broken rod end from incident engine (NLR code S)	11
3.1.1 Macrofractography	11
3.1.2 Microfractography	11
3.1.3 Fatigue striation counts	11
3.1.4 "Flight by-flight" or peak load striation counts	12
3.2 Broken-open spherical rod end from incident engine (NLR code S)	12
3.2.1 Macrofractography	12
3.2.2 Microfractography	13
3.3 Broken-open spherical rod end from incident engine (NLR code S <sub>1</sub> )	13
3.3.1 Macrofractography	13
3.3.2 Microfractography	13
3.4 Broken-open spherical rod end from another engine (NLR code A)	13
3.4.1 Macrofractography	14
3.4.2 Microfractography	14
3.5 LCF specimens from IEPG TA 31	14
3.5.1 Macrofractography	14
3.5.2 Microfractography	15
<b>4 Dimensions and surface roughness</b>	<b>16</b>
4.1 Mod radii	16
4.2 Diameters	16
4.3 Surface roughness	18
<b>5 Fretting and binding</b>	<b>20</b>
<b>6 Sleeves from the incident engine</b>	<b>21</b>
<b>7 Microstructures and hardness</b>	<b>22</b>
7.1 Microstructures	22
7.2 Hardness	22



<b>8</b>	<b>Interference colours on fracture surfaces</b>	<b>23</b>
8.1	Oxidation of metallic surfaces	23
8.2	Interference colours on the fatigue fracture surfaces	23
8.2.1	Broken rod end from incident engine (NLR code S)	23
8.2.2	Broken-open spherical rod end from incident engine (NLR code S)	24
8.2.3	Broken-open spherical rod end from incident engine (NLR code S <sub>1</sub> )	24
8.2.4	Broken-open spherical rod end from another engine (NLR code A)	24
8.2.5	LCF specimens from IEPG TA 31	24
8.3	Interference colours due to furnace oxidation of fatigue fracture surfaces	24
8.4	Comparison of furnace oxidation with the broken rod end (NLR code S)	25
<b>9</b>	<b>Estimates of stresses on the broken rod end (NLR code S)</b>	<b>26</b>
9.1	Tensile and bending stresses: derivation from operating conditions	26
9.1.1	Tensile stress in the rod	26
9.1.2	Contact stress due to pressure on the spherical ends	26
9.1.3	Swivelling moment on the spherical ends under pressure	27
9.1.4	Tensile + bending stress in the rod	27
9.1.5	Summary	27
9.2	Fatigue stresses: derivation from the Stage I → Stage II transition	28
<b>10</b>	<b>Discussion</b>	<b>30</b>
10.1	Fracture surface interpretation	30
10.1.1	Fractography	30
10.1.2	Interference colours	30
10.1.3	Engine operating history and fracture surface details	31
10.2	Source of the bending fatigue	32
10.3	Dimensions and surface roughness	32
10.4	Microstructures and hardness	33
10.5	Vendor source	33
<b>11</b>	<b>Conclusions and recommendations</b>	<b>34</b>
11.1	Conclusions	34
11.2	Recommendations	34
<b>12</b>	<b>References</b>	<b>36</b>

5 Tables

50 Figures

(87 pages in total)



## Nomenclature

$\alpha$	: contact angle
A, $A_1$ , $A_2$	: radii
AMS	: Aerospace Material Specification (issued by the ASTM and SAE)
ASTM	: American Society for Testing and Materials
$D_1$	: cap diameter of the air supply tube expansion sleeve
$D_2$	: diameter of the air supply manifold support rod
DOF	: Direction Of Flight
EDX	: Energy Dispersive analysis of X-rays
EOT	: Engine Operating Time
$\eta$	: coefficient of friction
F	: force
h	: projected height of contact area
I	: second moment of area
K	: stress intensity factor
$K_{\max}$	: maximum stress intensity factor
$\Delta K_{\text{eff}}$	: effective stress intensity factor range
LCF	: Low Cycle Fatigue
LTF	: specimen code (together with number) for IEPG TA 31 low cycle fatigue tests
M	: swivelling moment
MFG	: manufacturing
NASA/FLAGRO	: computer code for fatigue crack growth prediction
$N_f$	: number of cycles to failure
P	: pressure
$r_y^c$	: cyclic plastic zone size
R	: stress ratio ( $\sigma_{\min}/\sigma_{\max}$ )
R, $R_1$ , $R_2$ , $R_3$	: radii
$R_A$ , $R_{\max}$ , $R_Z$	: surface roughness parameters
SAE	: Society of Automotive Engineers
SEM	: Scanning Electron Microscope
$\sigma$ , $\sigma_{\max}$ , $\sigma_{\min}$	: stress, maximum stress, minimum stress
$\sigma_b$ , $\sigma_c$ , $\sigma_t$	: bending stress, contact stress, tensile stress
$\sigma_{\text{tmax}}$	: maximum tensile stress
$\sigma_y^c$	: cyclic yield stress
T.O.	: Technical Order (for maintenance)



## 1 Introduction

In 1995 an in-flight fire warning occurred in a high-performance aircraft. Post-flight investigation showed that an air supply manifold support rod, part of the engine's high pressure compressor bleed air assembly, had fractured to cause local damage and discoloration of the airframe.

Figure 1 shows the broken rod *in situ*. Normally the rod held together two expansion sleeves connecting the engine's diffuser case air supply tube with the bleed air supply manifold. Fracture of the rod resulted in separation of the expansion sleeves, visible in figure 1, and impingement of hot bleed air on the surrounding airframe.

Figure 2 shows where the broken rod was located with respect to the diffuser case, namely at the 8 o'clock position looking in the direction of flight (DOF). A second, unbroken rod was located at the 4 o'clock position. Figure 3 gives a full-size sketch of an air supply manifold support rod and also shows the location of fracture in the broken rod.

The rod material was Inconel 718 conforming to AMS 5663, i.e. rolled or forged products, with the same standard heat treatment used for the Inconel 718 pancake forgings of the IEPG TA 31 programme (Ref. 1). This heat treatment results in Rockwell hardnesses with a typical range of C40 - C47.

The engine operating history for the broken air supply manifold support rod is given below. According to the T.O., each maintenance would have involved loosening and re-tightening the expansion sleeves. Normally this should allow arbitrary rotation of each rod about its longitudinal axis.

	EOT (hours)		LCF (cycles)		Flights	
	Cumulative	Interval	Cumulative	Interval	Cumulative	Interval
1st Maintenance	410.9	761.5	2361	3082	257	326
2nd Maintenance	1172.4		5443		583	
Rod Failure	1315.9	143.5	5786	343	640	57

Information from the engine manufacturer indicated that the operating environment for the air supply manifold support rods is high pressure bleed air typically at temperatures of 550 °C - 560 °C. However, the bleed air temperature can reach 668 °C under extreme conditions, although this would be for short periods only.



Apart from the high air pressure, which is unlikely to affect the fracture properties of Inconel 718 (Ref. 2), the material, environmental and life-cycle conditions for the broken air supply manifold support rod were similar to those for LCF specimens in the IEPG TA 31 programme (Ref. 3). Thus it was found that diagnostic aspects of the rod failure were aided by LCF tests from the IEPG TA 31 programme.

## 2 Scope of the failure investigation

The scope of the failure investigation was as follows:

- Fractography
  - broken rod end from incident engine
  - forcibly opened cracks at spherical rod ends of
    - broken and unbroken rods from incident engine
    - another rod
    - LCF specimens from IEPG TA 31
- Dimensions, Surface Roughness
  - broken and cracked rods
  - other rods
- Fretting and Binding
- Sleeves from the Incident Engine
- Microstructures and Hardness
- Interference Colours on Fracture Surfaces
- Estimates of Stresses
  - tensile and bending stresses: derivation from operating conditions
  - fatigue stresses: derivation from Stage I → Stage II fatigue transition
- Discussion
- Conclusions and Recommendations

Table 1 on the next page lists the air supply manifold support rods examined in the investigation.



Table 1 Key to codes for air supply manifold support rods

NLR code	Position on engine	MFG date code	Approximate LCF cycles	Remarks
S	8 hr	59	5786	broken rod end broken-open spherical rod end
S <sub>1</sub>	4 hr	59	5786	broken-open spherical rod end
A	4 hr	59	6185	broken-open spherical rod end
B	8 hr	59	6185	—
C	8 hr	67	8395	—
D	4 hr	67	8395	—
E	4 hr	123	10,295	—
F	—	123	—	new
G	—	39	—	} rods from an NLR diffuser case } investigation in 1994
H	—	39	—	

### 3 Fractography

#### 3.1 Broken rod end from incident engine (NLR code S)

##### 3.1.1 Macrofractography

Figure 4 shows the as-received macroscopic appearance of the fracture surface of the broken rod end. Figure 5 is a schematic of the broad divisions of interference colours and fatigue fracture characteristics. There are two main locations of fatigue initiation and crack growth. The older fatigue area, which shows 2nd order interference colours, see section 8, is centred on the 2 o'clock position as viewed in figures 4 and 5. The more recent and main crack, which shows 1st order interference colours, see section 8, is centred on the 6 o'clock position. The shapes of the early crack fronts are diagnostic for fatigue controlled by bending stresses rather than axial stresses. Evidence for this is given in subsection 3.5.1.

##### 3.1.2 Microfractography

Figure 5 indicates that the main crack initiated by Stage I fatigue. In fact, this is inferred from the rough fracture topography, figure 6, and observation of similar topographies on less oxidised fatigue fracture surfaces of a broken-open rod (NLR code A) from another engine, see subsection 3.4.2, and also the fatigue fracture surfaces of LCF specimens from the IEPG TA 31 programme, see subsection 3.5.2.

The need for inferring Stage I fatigue for the broken rod end is severe oxidation of the initial silver-coloured fracture surface of the main crack, figure 7. It should be noted that Stage I fatigue is common in precipitation-strengthened nickel-base superalloys, like Inconel 718, and occurs in both LCF and high cycle fatigue (Ref. 4).

Figure 8 shows the Stage I → Stage II fatigue transition at low magnification in the Scanning Electron Microscope (SEM). The change in fracture topography is evident, and "beach marks" representing positions of the Stage II fatigue crack front are also visible. Figure 9 is a detail of the Stage II fracture surface, showing fatigue striations.

##### 3.1.3 Fatigue striation counts

Numerous measurements of fatigue striation spacings were made in order to obtain a cycle count in the Stage II area. To improve the resolution in the SEM the fracture surface was sputter coated with a very thin layer of gold. The results are shown in figure 10. The total cycle count for the Stage II area was estimated to be about 14,500 cycles. A significant feature of the measurements is the very gradual increase in striation spacings. This is unusual over such a wide range in crack length and raised doubts as to the usefulness of measuring striation spacings

*per se.*

#### **3.1.4 "Flight by-flight" or peak load striation counts**

The fatigue fracture surface of the broken rod end was mapped completely at low to intermediate SEM magnifications ( $\times 200$  -  $\times 1000$ ) and at a tilt angle of  $25^\circ$  to improve the visibility of crack front markings. The mapping revealed periodic large striations, sometimes ill-defined, that might correspond to the relatively large upward load excursions when starting the engine, but in any event most probably represent peak load excursions.

Measurements of the distances between large striations were made by two of the investigators (RJHW, HNH). The results are shown in figure 11 as plots of the cumulative number of large striations with crack depth. The positions of the broad divisions of interference colours are indicated also. If the distances between large striations did correspond to the relatively large upward load excursions when starting the engine, then these distances would represent flight-by-flight increments of crack growth. In that case, figure 11 would represent a Stage II fatigue life of about 260 flights.

However, as will be discussed in section 10, our opinion is that the large striations represent peak load excursions that occur more than once per flight.

### **3.2 Broken-open spherical rod end from incident engine (NLR code S)**

Fluorescent penetrant inspection of the spherical rod end of the broken rod, NLR code S, from the incident engine indicated the presence of cracks in the radius blending into the spherical end. This main part of the broken rod was pulled in tension to forcibly open any actual cracks. The spherical rod end fractured at the transition from the radius to the shank, revealing three small fatigue cracks.

#### **3.2.1 Macrofractography**

Figure 12 shows the macroscopic appearance of the fracture surface of the broken-open spherical rod end, together with a schematic of interference colours on the fatigue fracture surfaces. The shapes of the broken-open fatigue cracks suggest their initiation and growth were controlled by bending stresses. All the cracks show 2nd order interference colours, see section 8.

Figure 13 shows the relative positions, viewed in the outboard direction, of the cracks in the broken/broken-open parts of the rod. There is some correlation, notably between the main crack at the broken end and two of the cracks in the broken-open end. If anything, this correlation indicates that tensile bending stresses at and near the 6 o'clock position in figure 13 may have been responsible for initiating these cracks.



### 3.2.2 Microfractography

The fatigue fracture surfaces were considerably oxidised. Stage I → Stage II fatigue transitions were inferred from a change in fracture topography similar to that observed for a broken-open rod from another engine, see subsection 3.4.2. An example of this transition, for the crack at the 4 o'clock position of figure 12, is given in figure 14; and figure 15 is a detail of the Stage II area, showing oxidised fatigue striations.

### 3.3 Broken-open spherical rod end from incident engine (NLR code S<sub>1</sub>)

The second rod from the incident engine was inspected with fluorescent penetrant. Five crack indications were obtained in the transition from the radius to the shank at the spherical end. The rod was subsequently pulled in tension to forcibly open the cracks. The rod fractured over four of the five indicated cracks. In addition, two previously undetected cracks were found in the same radius, their detection being made possible by the forcible overload.

#### 3.3.1 Macrofractography

Figure 16 shows the macroscopic appearance of the fracture surface of the broken-open spherical rod end, together with a schematic of interference colours on the fatigue fracture surfaces and the locations of the side surface cracks. The shapes of the broken-open fatigue cracks suggest their initiation and growth were controlled by bending stresses. They are, however, fairly evenly distributed around the circumference of the fracture surface.

Figure 17 shows two of the side surface cracks, which had been partly opened-up by the forcible overload: the left-hand crack in figure 17 had been indicated by fluorescent penetrant inspection before the rod was pulled in tension. The cracks were exactly at an abrupt change in the mod radius.

#### 3.3.2 Microfractography

The fatigue fracture surfaces were considerably oxidised. Stage I → Stage II fatigue transitions were inferred from a change of fracture topography similar to that observed for a broken-open rod from another engine, see subsection 3.4.2. An example of this transition, for the crack at the 4 o'clock position in figure 16, is given in figure 18. Figure 19 is a detail of the Stage II area for the crack at the 7 o'clock position in figure 16, showing oxidised fatigue striations just before the forcible overload.

### 3.4 Broken-open spherical rod end from another engine (NLR code A)

Several unbroken rods, NLR codes A - H, see table 1, were obtained and inspected by fluorescent penetrant. One of these rods, NLR code A, gave crack indications in the radius blending into the spherical end. The rod was subsequently pulled in tension to forcibly open any actual cracks. The spherical rod end fractured at the blending radius, revealing five cracks, two

of which had coalesced.

### 3.4.1 Macrofractography

Figure 20 shows the macroscopic appearance of the fracture surface of the broken-open spherical rod end, together with a schematic of the interference colours and fracture characteristics. The rod fractured over all the indicated cracks. The shapes of the broken-open fatigue cracks suggest their initiation and growth were controlled by bending stresses.

### 3.4.2 Microfractography

Figure 21 is a low magnification SEM fractograph of the broken-open spherical rod end: this is the mating fracture surface to that shown in figure 20. The main crack at the 6 o'clock position in figures 20 and 21 showed a change in fracture topography corresponding to the Stage I → Stage II fatigue transition. However, as in the case of the rods from the incident engine, the occurrence of Stage I fatigue is inferred from the rough fracture topography, since the initial cracked area was severely oxidised, figure 22.

On the other hand, the crack at the 3 o'clock position in figure 21 was less oxidised (this crack is at the 9 o'clock position in Fig. 20). Figures 23 and 24 give details of this crack, including the Stage I → Stage II fatigue transition. The characteristics of Stage I fatigue are most clearly seen at the centre of figure 24, namely flat and crystallographically ridged facets: see also subsection 3.5.2. The characteristics of Stage II fatigue were fatigue striations. Examples are given in figure 25.

Energy dispersive X-ray (EDX) spot analyses were made at the origins of all the fatigue cracks shown in figures 20 and 21. The spectra obtained were typical for Inconel 718 base material: there was no evidence for an association between fatigue origins and niobium carbide (NbC) particles.

## 3.5 LCF specimens from IEPG TA 31

### 3.5.1 Macrofractography

Figure 26 gives examples of LCF fracture surfaces resulting from IEPG TA 31 tests at the NLR. These tests were done under tension-compression loading, and the shapes of the fatigue crack fronts are very different from those observed for the air supply manifold support rods. In particular, the crack fronts in figure 26 have positive (convex-outward) curvatures, while figure 4 shows negative (concave-outward) curvatures for much of the fatigue fracture surface. Also, the small cracks in figure 26 (specimen LTF 53) have much more positive curvatures than the small cracks in figures 12, 16 and 20.

These differences in crack front curvatures between the LCF specimens and the air supply manifold support rods are considered to be due to different fatigue loading conditions, namely axial tension-compression fatigue loading for the LCF specimens, and predominantly bending fatigue loading for the rods.

### 3.5.2 Microfractography

The fracture surface of specimen LTF 110, see figure 26, was examined in detail. This specimen had been tested with HOT TURBISTAN, a standardised load sequence for turbine discs that is broadly representative for the load sequences on some other engine components, including the air supply manifold support rods in the present investigation.

Figure 27 is an intermediate magnification SEM fractograph of the fatigue initiation area for specimen LTF 110, showing a transition from Stage I to Stage II fatigue. Figure 28 is an EDX mapping of the same area with the detector set for niobium. This figure shows that fatigue initiated at a large NbC particle.

Figures 29 and 30 show details of the Stage I and Stage II fatigue, respectively. The characteristics of Stage I fatigue were flat and crystallographically ridged facets, as observed clearly for one of the broken-open spherical rod ends, see figure 24 and subsection 3.4.2. The characteristics of Stage II fatigue were fatigue striations.



## 4 Dimensions and surface roughness

### 4.1 Mod radii

Figures 31-33 give the mod radii  $R_1$  and  $R_2$  measured using a profile projector at a magnification  $\times 50$ . The table in figure 31 summarises the results as average radii. Note, however, from figures 32 and 33 that the radius profiles consist of different radii, many with intermediate linear segments. There are also undercuts in some of the profiles.

The contours of the mod radii  $R_1$  and  $R_2$  were also measured. This was done by a specialist firm using a Mahr-Perten Perthometer S5P. The results are given in table 2. There are several points to note:

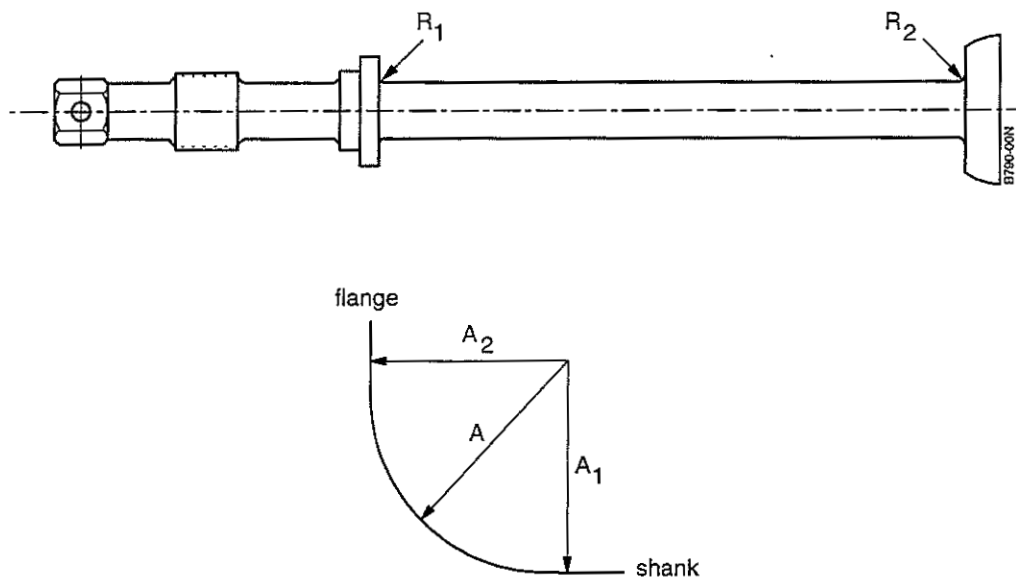
- (1) The nominal A values of  $R_1$  for the broken rod (S) and broken-open rods ( $S_1$ , A) were larger than those of the other rods: the values of A for rods B and F were especially small.
- (2) The undercut/overcut percentage variations of  $R_1$  for the broken rod (S) and broken-open rods ( $S_1$ , A) were not exceptional, especially in the light of the overall smaller values of A,  $A_1$  and  $A_2$  for rods B, C, E and F.
- (3) The nominal A values of  $R_2$  for the broken rod (S) and broken-open rods ( $S_1$ , A) were larger than the values for rods B and C, both of which had survived uncracked for greater numbers of cycles, see table 1.
- (4) The undercut/overcut percentage variation of  $R_2$  for the broken rod (S) was the largest of all the rods examined. This *may* have contributed to cracking in the radius/shank transition at the spherical end. However, the broken-open rod A had very uniform radius measurements but nevertheless cracked in service.

Summarising, the results do not provide any evidence that absolute and relative mod radius dimensions played a significant part in cracking of the rods.

### 4.2 Diameters

Figure 34 gives the diameter measurements made at the NLR. All measurements were within the specified tolerances.

Table 2 Mod radii contours for R<sub>1</sub> and R<sub>2</sub>



Radius location	Parameters	NLR code rods						
		S	S <sub>1</sub>	A	B	C	E	F
R <sub>1</sub>	A (mm)	1.630	1.486	1.526	1.086	1.262	1.394	0.834
	A <sub>1</sub> (mm)	1.699	1.522	1.530	1.130	1.255	1.352	0.865
	A <sub>2</sub> (mm)	1.531	1.399	1.407	1.034	1.207	1.287	1.004
	$\left  \frac{A - A_1}{A} \right $ (%)	4.2	2.4	0.3	4.1	0.6	3.0	3.7
	$\left  \frac{A - A_2}{A} \right $ (%)	6.1	5.9	7.8	4.8	4.4	7.7	20.4
R <sub>2</sub>	A (mm)	1.200	1.744	1.193	1.107	1.095	1.571	1.273
	A <sub>1</sub> (mm)	1.324	1.810	1.192	1.138	1.117	1.498	1.217
	A <sub>2</sub> (mm)	1.177	1.629	1.201	1.107	1.044	1.521	1.299
	$\left  \frac{A - A_1}{A} \right $ (%)	10.3	3.8	0.1	2.8	2.0	4.6	4.4
	$\left  \frac{A - A_2}{A} \right $ (%)	1.9	6.6	0.7	0	4.7	3.2	2.0



### 4.3 Surface roughness

In the first instance the radii of the rods with NLR code S, S<sub>1</sub>, A-H (see Tab. 1) were examined with a stereobinocular and compared with a standard roughness plate, RuGo test No. 1. The roughness appearances of all the rods were intermediate between the roughnesses 32 μin. and 63 μin. on the RuGo test No. 1. This is less than the average roughness limit of 125 μin. specified by the engine manufacturer.

Secondly, the roughnesses were measured by a specialist firm using a Mahr-Perten Perthometer S5P. Figure 35 shows the locations of the roughness measurements and how they were made. The results are given in table 3 in terms of the following roughness parameters:

- R<sub>max</sub> : maximum roughness height (peak-to-valley) over five consecutive measurements.
- R<sub>Z</sub> : average roughness height (peak-to-valley) over five consecutive measurements.
- R<sub>A</sub> : average roughness height/depth variation from a mean line.

Table 3 Mod radii roughnesses for R<sub>1</sub>, R<sub>2</sub>, R<sub>3</sub>

Radius location	Parameters	NLR code rods						
		S	S <sub>1</sub>	A	B	C	E	F
R <sub>1</sub>	R <sub>max</sub> (μin.)	138	360	218	194	114	170	114
	R <sub>Z</sub> (μin.)	113	170	169	147	102	140	93
	R <sub>A</sub> (μin.)	17	29	35	29	17	33	17
R <sub>2</sub>	R <sub>max</sub> (μin.)	224	207	165	120	253	118	174
	R <sub>Z</sub> (μin.)	140	161	138	104	150	105	143
	R <sub>A</sub> (μin.)	28	30	22	19	26	17	37
R <sub>3</sub>	R <sub>max</sub> (μin.)	68	121	103	114	86	236	238
	R <sub>Z</sub> (μin.)	57	94	72	81	76	127	203
	R <sub>A</sub> (μin.)	11	15	15	16	12	20	42



There are several points to note from table 3:

- (1) The average roughness,  $R_A$ , for all the rods is well within the average roughness limit of 125  $\mu\text{in.}$  specified by the engine manufacturer.
- (2) In view of the fact that  $R_{\text{max}}$  and  $R_Z$  are more relevant to fatigue strength than  $R_A$ , the surface roughness of the broken rod (NLR code S) is not especially high at the  $R_1$  location, which was where fracture occurred.
- (3) The  $R_{\text{max}}$  and  $R_Z$  values for the rods S,  $S_1$  and A at the spherical end, i.e. mod radius  $R_2$ , are relatively high. This *may* help to explain the occurrence of cracks at the  $R_2$ /shank transitions of these rods. However, the uncracked rod C had the highest values of  $R_{\text{max}}$  and  $R_Z$ , and - as shown in table 1 - a longer cyclic life than the rods S,  $S_1$  and A.

Summarising, the results do not indicate that surface roughness played a major part in fracture of the rod S at the  $R_1$ /shank transition. However, it could have contributed.



## 5 Fretting and binding

There was evidence of local fretting on the spherical ends of the rods listed in table 1, except of course the new rod (NLR code F). Figures 36-39 give examples for the broken and broken-open rods (NLR code S, S<sub>1</sub>, A) and an uncracked rod (NLR code D). If anything, the amount of fretting on the spherical end of the older, uncracked rod (Fig. 39) was more than on the other spherical ends.

The T.O. specifies that the air supply manifold support rods must be installed with an anti-galling compound (molybdenum disulphide + binder) applied to the spherical contact surfaces of the expansion sleeves. In the engine manufacturer's specification it is stated that this anti-galling compound is primarily to reduce galling and wear on parts operating at temperatures up to 400 °C ; and in certain anti-seize applications this compound is useful on parts operating at temperatures up to 649 °C. However, in a NAVAIR T.O. (Ref. 5) it is stated that molybdenum disulphide is not stable above 427 °C and should not be used in locations where operating temperatures could be higher.

The spherical rod end of the broken rod (NLR code S) from the incident engine was subjected to surface analysis using Energy Dispersive analysis of X-rays (EDX). Figure 40 compares the spherical end analysis with a reference analysis of the rod. The relative heights of the peaks labelled Mo indicate that anti-galling compound had been applied to the spherical end (note that a peak due to sulphur would be masked by the molybdenum).

In addition to the foregoing evidence and information, 28 air supply manifold support rods that had seen service were investigated, and a number showed evidence of fretting on the spherical ends. Also, inspection of 5 engines revealed one rod to be immovable.

Summarising, it may be concluded that at least some air supply manifold support rods experience binding in service, such that they are no longer able to provide accommodatory swivelling at the spherical ends. Based on information from the engine manufacturer it may be expected that during engine start-up the rods reach temperatures well above 500 °C. This means that even during the first start-up after engine assembly/reassembly the anti-galling compound could decompose and cease to function. In other words, it is possible that some air supply manifold support rods become immovable soon after the engine is in operation. This possibility is discussed further in sections 9 and 10.



## **6 Sleeves from the incident engine**

The air supply tube expansion sleeves from the 8 o'clock position on the incident engine, see figure 2, showed evidence of relative movement of the inner and outer sections of the air supply assembly. Figure 41 gives views of the inside ring surfaces of the sleeves, which had been connected in service by the broken rod (NLR code S). These views show grooves, especially on the manifold side, that were non-concentric with the ring axes.



## 7 Microstructures and hardness

### 7.1 Microstructures

The microstructures of several air supply manifold support rods, including the broken rod (NLR code S) from the incident engine, were examined by optical metallography and using Bereha's tint etch. Examples are given in figures 42-46. The basic microstructures were typical for standard heat-treated Inconel 718.

The grain sizes of the metallographically examined rods were measured by the intercept method. Table 4 gives the approximate ASTM grain sizes. There was quite a wide range in grain size, ASTM 9.5 - 12.8. The material from the broken rod (NLR code S) was relatively fine grained.

Table 4 Grain sizes for several air supply manifold support rods

Rod codes		Remarks	ASTM G.S. number	Rod codes		Remarks	ASTM G.S. number
NLR	MFG date code			NLR	MFG date code		
S	59	broken	11.6	F	129	new rod	12.8
B	59		11.2	G	39		9.5
E	123		10.5				

### 7.2 Hardness

Rockwell hardness values for several air supply manifold support rods, including both rods from the incident engine (the broken rod, NLR code S, and the broken-open rod, NLR code S<sub>1</sub>), are given in table 5. The hardness values are the averages of three measurements for each rod. The Aerospace Structural Metals Handbook (Ref. 6) quotes hardness values with a typical range of C40 - C47 for a wide variety of Inconel 718 products in the standard heat-treated condition. It may be concluded that there is nothing untoward about the hardnesses of the rods from the incident engine.

Table 5 Rockwell C hardness for several air supply manifold support rods

Rod codes		Remarks	Rockwell C hardness	Rod codes		Remarks	Rockwell C hardness
NLR	MFG date code			NLR	MFG date code		
S	59	broken broken-open broken-open	42.0	E	123	new rod	40.0
S <sub>1</sub>	59		46.7	F	129		39.8
A	59		39.7	G	39		38.8
B	59		41.2	H	39		38.7
D	67		39.5				

## 8 Interference colours on fracture surfaces

### 8.1 Oxidation of metallic surfaces

Figure 47 shows a textbook description of the sequence of interference colours produced by the oxidation of metallic surfaces. The left-hand side of this figure shows illustrative positions of interference bands as functions of the oxidation film thickness. The right-hand side of this figure shows the resulting colours, which can vary.

For the present investigation the significance of interference colours due to oxidation lies in their potential usefulness in estimating the elevated temperature exposure times for the fatigue fracture surfaces of the broken rod (NLR code S) and the broken-open spherical ends of the rods with NLR code S, S<sub>1</sub> and A.

There are several potential limitations to this diagnostic use of interference. These include any changes in fracture mechanism, fracture surface roughness, cycle frequency and effects of peak loads. However, except for a change in fracture mechanism, for example from transgranular fatigue cracking to intergranular dwell cracking in nickel-base superalloys, the other influences appear to be minor. The single most important influence on the interference colours is the exposure temperature (Ref. 8): it is essential to have a good estimate of the exposure temperature in order to estimate the exposure times. As mentioned in section 1, information from the engine manufacturer indicated that bleed air temperatures of 550 °C - 560 °C will be obtained except under extreme operating conditions. In turn, this means that the air supply manifold support rods operate at temperatures typically in the range 550 °C - 560 °C.

### 8.2 Interference colours on the fatigue fracture surfaces

#### 8.2.1 Broken rod end from incident engine (NLR code S)

Figures 4 and 5 show the as-received macroscopic appearance of the broken rod end and a schematic of the broad divisions of interference colours and fatigue fracture characteristics (Stage I and Stage II fatigue for the main crack). The secondary crack is older: it shows 2nd order interference colours down to blue at the outside surface. Under the influence of the main crack the secondary crack began to grow again from 2nd order yellow through the silvery hiatus to the 1st order colours blue, brown and finally yellow.

The main crack shows predominantly 1st order interference colours, notably in Stage II fatigue, see figures 4 and 5. An unusual aspect of these colours is the submacroscopic banding. These bands resemble, in shape and spacing, the beach marks on fatigue fracture surfaces produced under variable amplitude loading.



The submacroscopic interference colour bands undoubtedly portray crack front positions during the fatigue crack growth process. The question is: what do these crack front positions represent? This will be discussed in section 10.

#### **8.2.2 Broken-open spherical rod end from incident engine (NLR code S)**

Figure 12 shows the macroscopic appearance of the fracture surface of the broken-open spherical rod end, together with a schematic of interference colours on the fatigue fracture surfaces. All the cracks showed a colour sequence corresponding to 2nd order interference colours. This indicates that the cracks had been growing very slowly.

#### **8.2.3 Broken-open spherical rod end from incident engine (NLR code S<sub>1</sub>)**

Figure 16 shows the macroscopic appearance of the fracture of the broken-open spherical rod end, together with a schematic of interference colours on the fatigue fracture surfaces. For all the fatigue fracture surfaces the last parts were oxidised to a blue colour. This is most probably 1st order blue, which is next in sequence to the silvery hiatus, see figure 42. In any event, it is likely that the cracks were growing slowly.

#### **8.2.4 Broken-open spherical rod end from another engine (NLR code A)**

Figure 20 shows the macroscopic appearance of the fracture surface of the broken-open spherical rod end, together with a schematic of interference colours on the fatigue fracture surfaces. There were some variations in the successive positions of the colours, so that it is not certain whether some were 1st or 2nd order. However, the largest crack clearly shows the silvery hiatus followed by 1st order light blue. This crack was growing slowly at the time of its detection, and the other cracks were probably growing very slowly.

#### **8.2.5 LCF specimens from IEPG TA 31**

Figure 26 shows the macroscopic appearances of the fracture surfaces of three LCF specimens tested under the aegis of IEPG TA 31. All three fracture surfaces show predominantly 1st order interference colours. However, the fracture surface of specimen LTF 110 would have undergone longer elevated temperature exposure owing to dwell periods between simulated engine load cycles, and this is most probably the reason why the fatigue initiation area shows 2nd order yellow followed by the silvery hiatus. (Note that this is consistent with severe oxidation of the Stage I fatigue initiation area, see Fig. 29.)

### **8.3 Interference colours due to furnace oxidation of fatigue fracture surfaces**

From the IEPG TA 31 programme the NLR had available two Inconel 718 fatigue specimens that had fractured with large areas of Stage II fatigue crack growth at room temperature. The fracture surfaces were sectioned into slices which were exposed to air at 540 °C - 550 °C in an induction furnace for different times. The results are shown in figure 48. Within 1 hour the

initially grey (metallic) fatigue fracture surfaces oxidised to a straw yellow colour. Within 24 hours a dark blue colour began to dominate. Thereafter the rate of colour change decreased considerably, as would be expected from general considerations of the oxidation kinetics of metals at elevated temperatures (Ref. 9).

#### **8.4 Comparison of furnace oxidation with the broken rod end (NLR code S)**

Figure 49 compares a selection of the interference colours in figure 48 with the colours on the fracture surface of the broken rod (NLR code S) from the incident engine. The similarity of the colours and the sequence of colours (all 1st order) is evident. The times by which particular colours are obtained will not be exactly the same for furnace oxidation and the broken rod. However, these times should be similar in magnitude, for the following reasons:

- (1) Similar temperatures (540 °C - 550 °C for furnace oxidation; 550 °C - 560 °C operating temperatures for air supply manifold support rods, see subsection 8.1).
- (2) Similar fatigue fracture topography and roughness,
- (3) The likelihood that the overpressure of the bleed air (up to 25 bar) will have little or no effect on crack tip oxidation kinetics. This assertion is based on the fact that it is the *partial* pressure of oxygen that controls the crack tip oxidation of Inconel 718 (Ref. 10) and not the absolute pressure. (Be that as it may, if the bleed air overpressure were to have an effect on the oxidation kinetics, this effect would be to increase the rate of oxidation and shorten the times by which particular colours are obtained.)

Summarising, from a comparison of interference colours it seems likely that the period of Stage II fatigue for the broken rod (NLR code S) from the incident engine was no longer than 200 hours, and probably significantly shorter.

## 9 Estimates of stresses on the broken rod end (NLR code S)

### 9.1 Tensile and bending stresses: derivation from operating conditions

An air supply manifold support rod connects the diffuser case air supply tube expansion sleeve, see figure 2, via a transfer tube to the sleeve in the connector tube air supply manifold. During assembly the transfer tube can slide within the sleeves to avoid axial fit-up stresses in the rod. Also, the rod has two spherical ends, one of which is integral and the other fitted-on. These spherical ends fit into spherical seatings in the sleeves, with the intention of enabling any relative movement of the inner and outer sections of the air supply assembly to be compensated for. Thus at ambient temperature and pressure (engine off) there should be no loads on the rod.

#### 9.1.1 Tensile stress in the rod

When the engine is started the air supply manifold becomes pressurized to a maximum of 25 bar. The air supply manifold support rod is then under tensile stress owing to the air pressure. The tensile stress is given by  $P(D_1/D_2)^2$ , where  $P$  is the pressure,  $D_1$  is the internal diameter of the sleeve cap, and  $D_2$  is the rod diameter. Assuming  $P = 25 \text{ bar} = 25 \times 0.101325 \text{ MPa}$ ,  $D_1 = 68 \text{ mm}$  and  $D_2 = 8 \text{ mm}$ , the maximum tensile stress in the rod,  $\sigma_{\text{tmax}}$ , is given by

$$\sigma_{\text{tmax}} = (68/8)^2 \times 25 \times 0.101325 \text{ MPa} = 183 \text{ MPa} \quad (1)$$

This is a low value of tensile stress relative to the tensile and fatigue strengths of standard heat-treated Inconel 718.

#### 9.1.2 Contact stress due to pressure on the spherical ends

Consider the sketch opposite:

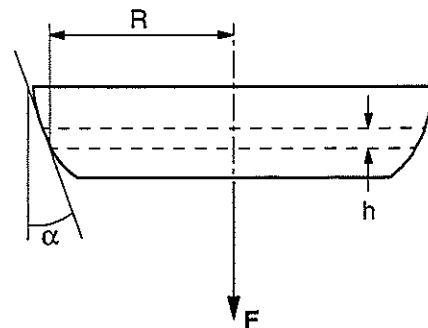
$$F = \frac{\pi}{4} (D_2)^2 \times \sigma_t \quad (2)$$

The contact stress is

$$\sigma_c = F / (\sin \alpha \times 2\pi R h) \quad (3)$$

With  $\alpha = 27^\circ$ ,  $h \sim 1 \text{ mm}$  and an average  $R = 10.25 \text{ mm}$ ,

$$\begin{aligned} \sigma_c &= F / (\sin 27^\circ \times 2\pi \times 0.01025 \times 0.001) \text{ MPa} \\ &= \left( \frac{\pi}{4} \times (0.008)^2 \times 183 \right) / (\sin 27^\circ \times 2\pi \times 0.01025 \times 0.001) \text{ MPa} \\ &= 315 \text{ MPa} \end{aligned} \quad (4)$$





This contact stress is substantial and means that under pressure the spherical ends may not be able to move freely in their seatings, depending on the friction.

### 9.1.3 Swivelling moment on the spherical ends under pressure

Since the spherical ends experience a considerable contact pressure, there is a moment required to move them. The swivelling moment  $M$  towards the rod axis is given by

$$M = 2\eta FR / (\pi \tan \alpha) \quad (5)$$

where  $\eta$  is the coefficient of friction and  $F$ ,  $R$  and  $\alpha$  are defined in subsection 9.1.2. Typical values of  $\eta$  with only slight fretting or marking of the contact surfaces are  $\eta = 0.2 - 0.3$ .

Assuming  $\eta = 0.2$ ,

$$\begin{aligned} M &= 2 \times 0.2 \times F \times 0.01025 / (\pi \tan 27^\circ) \\ &= 23.56 \text{ N.m} \end{aligned} \quad (6)$$

### 9.1.4 Tensile + bending stress in the rod

The maximum stress in the rod is in the outermost fibre and is due to tension + bending. Specifically,

$$\begin{aligned} \sigma &= \sigma_t + \sigma_b \\ &= F / (\pi D_2^2 / 4) + M (D_2 / 2) / I \end{aligned} \quad (7)$$

Where  $I$  is the second moment of area equal to  $\pi (D_2)^4 / 64$ . Then

$$\begin{aligned} \sigma &= 183 \text{ MPa} + (23.56 \times 0.004) / [\pi (0.008)^4 / 64] \text{ Pa} \\ &= 183 \text{ MPa} + 469 \text{ MPa} \\ &= 652 \text{ MPa} \end{aligned} \quad (8)$$

### 9.1.5 Summary

The foregoing calculations show that a rather low, and in view of the fretting evidence, see section 5 and figures 36-39, probably conservative value of the coefficient of friction,  $\eta = 0.2$ , enables a maximum stress of about 650 MPa to be reached in the rod before it will swivel to accommodate any relative movement of the inner and outer sections of the air supply assembly during engine operation. In unfavourable circumstances (higher values of  $\eta$ ) the maximum stress before swivelling could be much higher.



A major and dominating contribution of bending stress provides an explanation of failure of the broken rod (NLR code S) from the incident engine, for two reasons:

- (1) The magnitude of stresses necessary to cause fatigue failure.
- (2) The shapes of the early crack fronts, see subsection 3.5.1.

The source of bending stresses is relative movement of the inner and outer section during engine operation, whereby accommodatory swivelling at the spherical ends of the rod is prevented. Swivelling is prevented because the contact stress due to air pressure is substantial, the coefficient of friction for the spherical ends/spherical seatings does not have to be high, and it is possible that the anti-galling compound ceases to function soon after engine assembly/reassembly, see section 5.

## 9.2 Fatigue stresses: derivation from the Stage I → Stage II transition

As discussed in subsection 3.1, the main crack in the broken rod end (NLR code S) from the incident engine initiated by Stage I fatigue. At a crack depth of 0.54 mm there was a transition to Stage II fatigue. Such transitions are common in precipitation-strengthened nickel-base superalloys, and according to Runkle and Pelloux (Ref. 4) these transitions are governed in part by the cyclic plastic zone size at the crack tip becoming larger than the grain size. Under nominally plane strain conditions the cyclic plastic zone has a "butterfly-wing" shape with its longest dimension,  $r_y^c$ , approximately normal to the path of the fatigue crack. From reference 11 we may write:

$$r_y^c = 0.05 \left( \Delta K_{\text{eff}} / \sigma_y^c \right)^2 \quad (9)$$

where  $\Delta K_{\text{eff}}$  is the effective stress intensity factor range in fatigue, and  $\sigma_y^c$  is the cyclic yield stress of the material. Let  $r_y^c$  equal the average grain diameter at the Stage I → Stage II fatigue transition. The average grain diameter can be derived from the grain size measurements, table 4, and for the broken rod (NLR code S) is equal to 6.5  $\mu\text{m}$ . An estimate of the cyclic yield stress at 550 °C can be obtained from references 12 and 13: the monotonic yield stress of Inconel 718 at this temperature is 1025 MPa, and the cyclic yield stress will be approximately 0.75 × the monotonic yield stress, i.e. 769 MPa. Substituting into equation (9) gives

$$\frac{0.0065}{1000} = 0.05 \left( \Delta K_{\text{eff}} / 769 \right)^2 \quad (10)$$



whence

$$\Delta K_{\text{eff}} = 8.77 \text{ MPa } \sqrt{\text{m}}$$

During engine operation the largest cycles (notably start-stop cycles) will have a stress ratio  $R(= \sigma_{\text{min}}/\sigma_{\text{max}}) = 0$ . For this stress ratio a plane strain calculation (Ref. 14) gives  $\Delta K_{\text{eff}} = 0.75 \Delta K = 0.75 K_{\text{max}}$ . Assuming that it is the largest regularly-occurring cyclic plastic zone that is important to the Stage I  $\rightarrow$  Stage II fatigue transition, then the maximum stress intensity factor at the transition is given by

$$K_{\text{max}} = \Delta K_{\text{eff}}/0.75 \tag{11}$$

$$= (8.77/0.75) \text{ MPa } \sqrt{\text{m}}$$

$$= 11.7 \text{ MPa } \sqrt{\text{m}}$$

Now consider the main crack shown in figures 4 and 5. At the Stage I  $\rightarrow$  Stage II transition the crack configuration may be approximated by a crack depth : length ratio of 0.06. Using the NASA/FLAGRO SC09 stress intensity solution for a partly annular surface flaw in bending (Ref. 15) a crack depth  $a = 0.54 \text{ mm}$  gives

$$K/\sigma = 0.048 \sqrt{\text{m}} \tag{12}$$

Substituting  $K_{\text{max}}$  from equation (11), and  $\sigma_{\text{max}}$  for  $\sigma$ ,

$$11.7/\sigma_{\text{max}} = 0.048 \sqrt{\text{m}} \tag{13}$$

whence

$$\sigma_{\text{max}} = 244 \text{ MPa}$$

We now have an estimate of the maximum fatigue stress,  $\sigma_{\text{max}}$ , at the Stage I  $\rightarrow$  Stage II transition. Of course there are several uncertainties, of which the most important is likely to be whether the transition corresponds to  $r_y^c$  becoming equal to the average grain diameter. It may be necessary for  $r_y^c$  to significantly exceed the average grain diameter, in which case  $\sigma_{\text{max}}$  would be higher.

Nevertheless, the order-of-magnitude estimate of  $\sigma_{\text{max}}$  is reasonable, and it is significantly less than the estimated maximum stress which can be reached before swivelling of the rod occurs, see subsections 9.1.4 and 9.1.5. In other words, the estimations in sections 9.1 and 9.2 are consistent with the hypothesis that bending stresses causing fatigue initiation and crack growth can occur in the rod because it is not able to swivel to accommodate relative movement of the inner and outer sections of the air supply assembly during engine operation.



## 10 Discussion

### 10.1 Fracture surface interpretation

#### 10.1.1 Fractography

From the fractographic results on the broken and broken-open rod ends and the IEPG TA 31 LCF specimens it is concluded that fatigue cracking of the rods was controlled by bending stresses.

An estimate of 14,500 cycles was obtained for the Stage II fatigue fracture of the main crack in the broken rod end (NLR code S) from the incident engine. This estimate was based on one fatigue striation representing one cycle. For the same fracture area the number of large fatigue striations was estimated to be about 260. Interpretation of these results is given in subsection 10.1.3.

#### 10.1.2 Interference colours

From the interference colours due to oxidation it is concluded that the secondary crack on the fracture surface of the broken rod end (NLR code S) from the incident engine was older than the main crack. It is also concluded that the main crack showed predominantly 1st order interference colours, notably in Stage II fatigue. Additional evidence for this contention is provided by figure 26: although these fracture surfaces were obtained at a relatively high temperature, 600 °C, the very short time to failure for the right-hand specimen (LTF 53) means that the colours must be 1st order.

Furnace oxidation tests at 540 °C - 550 °C (representative for the operating temperatures of air supply manifold support rods) followed the development of 1st order interference colours on fatigue fracture surfaces. Comparison of these colours with those for the main crack of the broken rod (NLR code S) from the incident engine is given in figure 49. This comparison leads to the conclusion that the period of Stage II fatigue for the broken rod (NLR code S) was no longer than 200 hours, and probably significantly shorter.

A significant detail for the main crack of the broken rod (NLR code S) from the incident engine is the presence of submacroscopic interference colour bands, see figure 4. These bands portray crack front positions during the fatigue crack growth process. Figure 26 shows that constant amplitude loading (specimens LTF 53 and LTF 56) does not produce these bands, but that HOT TURBISTAN loading (specimen LTF 110) does to a slight extent. However, there is a major difference between the service experience of the broken rod (NLR code S) and the test with specimen LTF 110: namely, the test was done at constant temperature, while the broken rod

would have experienced flight-by-flight heating and cooling.

It is possible that the submacroscopic interference colour bands on the fracture surface of the main crack of the broken rod (NLR code S) from the incident engine were caused partly by flight-by-flight heating and cooling. If this were so, counting the bands would enable an estimate of the number of flights involved in Stage II fatigue. This is discussed further in subsection 10.1.3.

### 10.1.3 Engine operating history and fracture surface details

Figure 50 summarises the most likely relationships between the fatigue fracture surface details and engine operating history of the broken rod (NLR code S) from the incident engine. The secondary crack ① was the first to occur: as discussed in subsections 3.1.1 and 8.2.1, the secondary crack ① is older than the main crack. We suggest that as a result of the 1st maintenance the rod experienced a rotation about its longitudinal axis such that further growth of the secondary crack ① was inhibited. Fatigue then initiated the main crack. This suggestion is based on the controlling influence of bending stresses on fatigue cracking in the rod.

Figure 50 gives two possibilities, A and B, for formation of the main crack in the rod. Irrespective of which possibility is considered, an essential point is that the 2nd maintenance would have resulted in reassembly with the rod in a similar position (rotational orientation with respect to its longitudinal axis) to that between the 1st and 2nd maintenances. Although this might seem unlikely, the alternative is that the main crack initiated and grew to failure during the relatively short period between 2nd maintenance and failure (143.5 engine operating hours). This is even more unlikely, since it would be incompatible with the fractographic and interference colour evidence.

Possibility A suggests that between the 1st and 2nd maintenances the fatigue crack initiated and grew in Stage I and part of Stage II, i.e. forming the fatigue fracture areas ② and ③ in figure 50. In this rationale area ③ ends at the anomalously blue crack fronts in the mauve/purple zone, see figure 4; and area ④ would be formed during the last period of 143.5 engine operating hours between 2nd maintenance and failure. The difficulty with this rationale is that it is incompatible with the interference colours on the fracture surface: 143.5 engine operating hours would have turned most of area ④ to a light blue/dark blue colour, see figures 48 and 49.

Possibility B suggests that between the 1st and 2nd maintenances the main fatigue crack initiated and grew in Stage I, i.e. forming most - or all - of the fatigue fracture area ② in figure 50. This leaves the period from 2nd maintenance to failure, 143.5 engine operating hours, as the



maximum amount of time to form the fatigue fracture areas ③ and ④. This is compatible with the interference colours on the fracture surface, see figure 49. Furthermore, there were about 55-60 submacroscopic interference colours bands on areas ③ and ④. This number is in close agreement with the number of flights (57) from second maintenance to failure, hence the suggestion in subsection 10.1.2 that these bands could be caused partly by flight-by-flight heating and cooling.

Summarising, we favour possibility B, whereby Stage II fatigue crack growth took place between 2nd maintenance and failure, and comprised a maximum of 57 flights. This means that the number of large fatigue striations in Stage II fatigue (estimated to be about 260, see subsections 3.1.4 and 10.1.1) corresponds to a maximum of 57 flights. Consequently the large striations are considered to represent peak load excursions that occur more than once per flight. This is reasonable for high performance aircraft gas turbines. Also, the number of large fatigue striations agrees on an order-of-magnitude basis with the number of LCF counts (343) between 2nd maintenance and failure.

## **10.2 Source of the bending fatigue**

In section 5 evidence was presented for the occurrence of fretting and binding of air supply manifold support rods. Section 6 provided evidence of relative movement of the inner and outer sections of the air supply assembly, namely grooves on the inside ring surfaces of the air supply tube expansion sleeves surrounding the broken rod (NLR code S) from the incident engine.

Given the foregoing evidence, and also the magnitudes and self-consistency of the estimated tensile and bending stresses in section 9, it is reasonable to conclude that bending stresses causing fatigue initiation and crack growth in the rod (NLR code S) were due to the rod being unable to swivel to accommodate relative movement of the inner and outer sections of the air supply assembly during engine operation. A contributory factor is likely to be decomposition of the anti-galling compound (molybdenum disulphide + binder) applied to the spherical contact surfaces. This decomposition, and hence loss of function, could have begun at temperatures well below the normal operating temperatures of the rod, see section 5.

## **10.3 Dimensions and surface roughness**

Section 4 gives the results of measuring important dimensions and surface roughness of a number of air supply manifold support rods, including the rods from the incident engine. There was no evidence that dimensional variations (mod radii and diameter differences) played a role in rod cracking. Nor did surface roughness play a major part in fracture of the broken rod (NLR code S).



Be that as it may, the finished condition of the rods leaves something to be desired, notably the occurrence of undercuts/overcuts and discontinuous changes in the mod radius profiles.

#### **10.4 Microstructures and hardness**

Section 7 examines the microstructures and hardness of several air supply manifold support rods, including the broken rod (NLR code S) from the incident engine. The basic microstructures and hardnesses are considered to be typical for standard heat-treated Inconel 718 products. Blocky NbC carbides were present in the microstructures, but this is normal. Detailed examination of fatigue cracks in a broken-open spherical rod end (NLR code A) showed no evidence of an association between fatigue origins and the NbC particles, see subsection 3.4.2.

#### **10.5 Vendor source**

Table 1 shows that all the rods containing cracks had the same MFG date code. However, from the present investigation there is no evidence to suggest that the rods from a particular vendor are more liable to crack than others.

## 11 Conclusions and recommendations

### 11.1 Conclusions

Investigation of a number of air supply manifold support rods, including both rods from the incident engine, and also the air supply tube expansion sleeves surrounding the broken rod from the incident engine, leads to the following conclusions:

- (1) The rod failed by bending fatigue. Bending was due to relative movement of the inner and outer sections of the air supply assembly, whereby accommodatory swivelling of the spherical ends of the rod in the spherical seatings of the sleeves was prevented by contact pressure, fretting and binding. A contributory factor is likely to be decomposition of the anti-galling compound (molybdenum disulphide + binder) applied to the spherical contact surfaces of the sleeves.
- (2) The main crack in the broken rod showed a transition from Stage I to Stage II fatigue. At the transition the crack had a depth of 0.54 mm and a circumferential length of 9 mm. The remaining fatigue life from this crack size to failure is thought to be a maximum of 57 flights, corresponding to 143.5 hours of engine operating time.
- (3) There was no evidence that dimensional variations (mod radii and diameter differences) played a role in rod cracking. Nor did surface roughness play a major part in fracture of the broken rod.
- (4) The basic microstructures and hardnesses of several rods, including the broken rod, were typical for standard heat-treated Inconel 718 products. Blocky niobium carbide (NbC) particles, which are normally present in the microstructures, were not associated with fatigue initiation sites in the rods.

### 11.2 Recommendations

In view of conclusion (1) in subsection 11.1, it was recommended to consider an alternative anti-galling treatment. Possibilities which immediately present themselves are hard chromium and electroless nickel plating. However, these have maximum temperature capabilities below the typical operating temperatures of the air supply manifold support rods (Refs. 16 and 17).

What is required is an anti-galling compound or thin coating (probably no more than 25  $\mu\text{m}$  thick) with temperature capability of at least 670 °C (about the maximum temperature of the bleed air, see subsection 8.1). We investigated these possibilities within the Netherlands, leading



to the following suggestions:

(1) Anti-galling compounds

- Molykote HSC - PLUS
  - Molykote P37
  - Never-Seez Formel LV; Tools BV, Amsterdam
- } Mavron BV, Alphen aan den Rijn

all with temperature capability exceeding 1000 °C.

(2) Coating

- Diamalloy 3001 plasma sprayed cobalt-base superalloy with temperature capability up to 980 °C; Sulzer Metco BV, Breda.

The plasma-sprayed coating is a less attractive option because it is more expensive and requires finishing by grinding and lapping.

Secondly, in view of the results of the fluorescent penetrant inspection of several air supply manifold support rods at the NLR (see subsections 3.2, 3.3 and 3.4) it was recommended to inspect the rods currently in service, as an addition to the specified maintenance procedure in the T.O. This additional inspection was well under way by the beginning of 1996.



## 12 References

1. Barnard, P.M., Macro examination of Inconel 718 discs supplied by S.N.E.C.M.A. for the TA 31 programme, Report 92-LAB-187, European Gas Turbines (1992): Lincoln, UK.
2. Wanhill, R.J.H.; Boogers, J.A.M., The effects of peak loads and underloads on dwell crack growth in Inconel 718 at 600 °C - contribution to IEPG TA 31: Lifing Concepts for Military Aero-Engine Components, NLR Report TP 93300 L, National Aerospace Laboratory NLR (1993): Amsterdam, The Netherlands.
3. Heuler, P., IEPG-TA 31 Working Group minutes of the 13th meeting at MTU München, Industrieanlagen-Betriebsgesellschaft (1992): Ottobrunn, Germany.
4. Runkle, J.C.; Pelloux, R.M., Micromechanisms of low-cycle fatigue in nickel-based superalloys at elevated temperatures, Fatigue Mechanisms, ASTM STP 675, American Society for Testing and Materials, pp. 501-527 (1979): Philadelphia, Pennsylvania, USA.
5. NAVAIR 02-1-517/T.O. 2-1-111/DMWR 55-2800-206, p. 21-2.
6. Aerospace Structural Metals Handbook, 1994 Edition, Vol. 4, Code 4103, p.1, CINDAS/USAF CRDA Handbooks Operation, Purdue University, West Lafayette, Indiana, USA.
7. Evans, U.R., The Corrosion and Oxidation of Metals, Second Supplementary Volume, Edward Arnold, p. 379 (1976): London, UK.
8. Radtke, T.C., Personal Communication from the Aeronautical and Maritime Research Laboratory (AMRL), Melbourne, Australia, 23 March 1993.
9. Evans, U.R., The Corrosion and Oxidation of Metals: Scientific Principles and Practical Applications, Edward Arnold, pp. 27-28 (1971): London, UK.
10. Andrieu, E.; Ghonem, H.; Pineau, A., Two-stage crack tip oxidation mechanism in alloy 718, Elevated Temperature Crack Growth, MD-Vol. 18, The American Society of Mechanical Engineers, pp. 25-29 (1990).
11. Wanhill, R.J.H.; Looije, C.E.W., Fractographic and microstructural analysis of fatigue crack growth in Ti-6Al-4V fan disc forgings, AGARD Engine Disc Cooperative Test Programme, AGARD Report 766 (Addendum), Advisory Group for Aerospace Research and Development, pp. 2-1—2-40 (1993): Neuilly-sur-Seine, France.
12. Heuler, P.; Bergmann, J., IEPG-TA 31 basic material properties of IN 718, Technical Note TAB-T-30/93, Industrieanlagen-Betriebsgesellschaft (1993): Ottobrunn, Germany.
13. Heuler, P., Life prediction for engineering rim specimens, Technical Note TAB-T-54/94, Industrieanlagen-Betriebsgesellschaft (1994): Ottobrunn, Germany.
14. Newman, J.C., Jr., A crack-closure model for predicting fatigue crack growth under aircraft spectrum loading, Methods and Models for Predicting Fatigue Crack Growth under Random Loading, ASTM STP 748, American Society for Testing and Materials, pp. 53-84 (1981): Philadelphia, Pennsylvania, USA.
15. Fatigue Crack Growth Computer Program NASA/FLAGRO Version 2.0, Annex 2 in ESACRACK User's Manual, ESA PSS-03-209 Issue 2, European Space Agency, January 1995: Paris, France.



16. Metals Handbook Ninth Edition, Volume 5 Surface Cleaning, Finishing, and Coating, American Society for Metals, pp. 170-187 and 219-243 (1982): Metals Park, Ohio, USA.
17. A Handbook of Protective Coatings for Military and Aerospace Equipment, TPC Publication 10, National Association of Corrosion Engineers, pp. 63-66 (1983): Houston, Texas, USA.



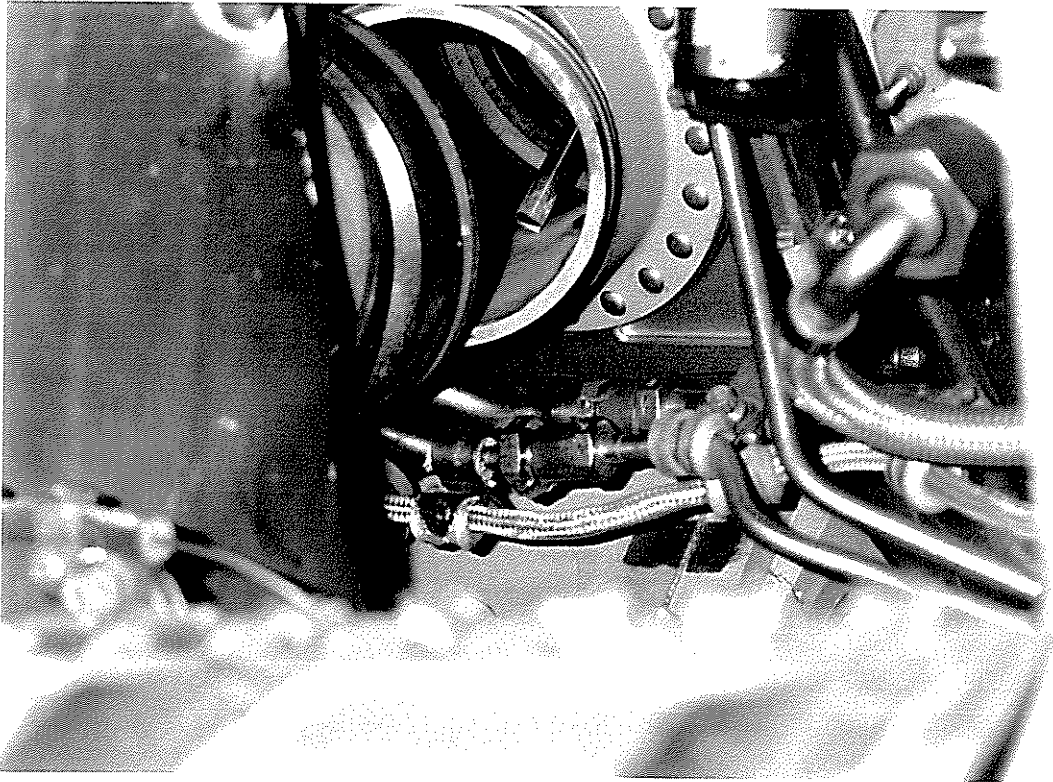


Fig. 1 The broken air supply manifold support rod in situ

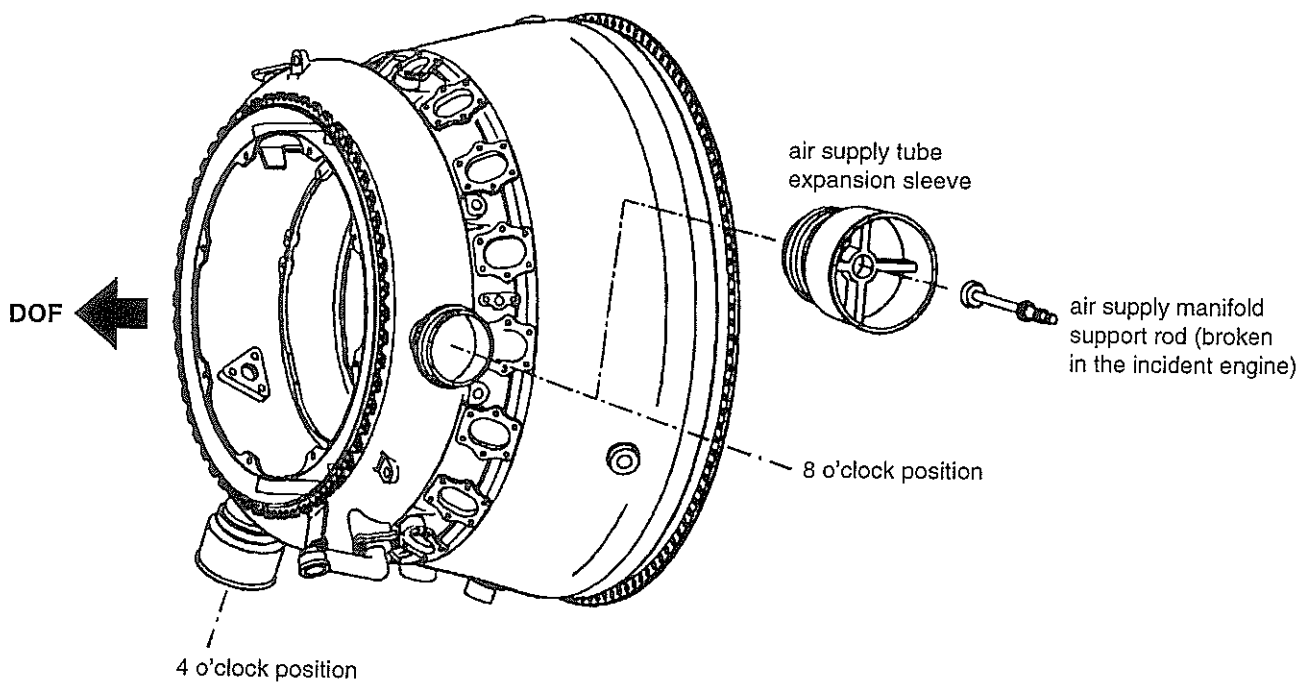
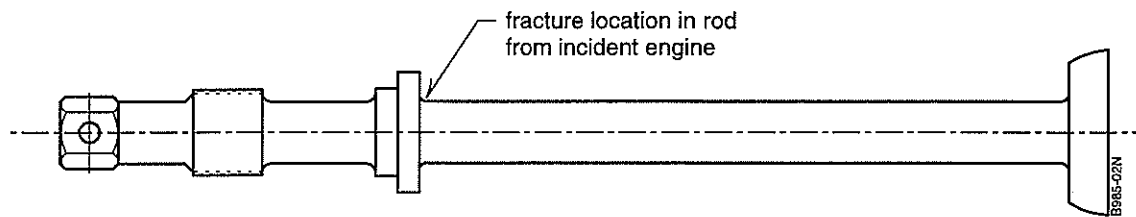
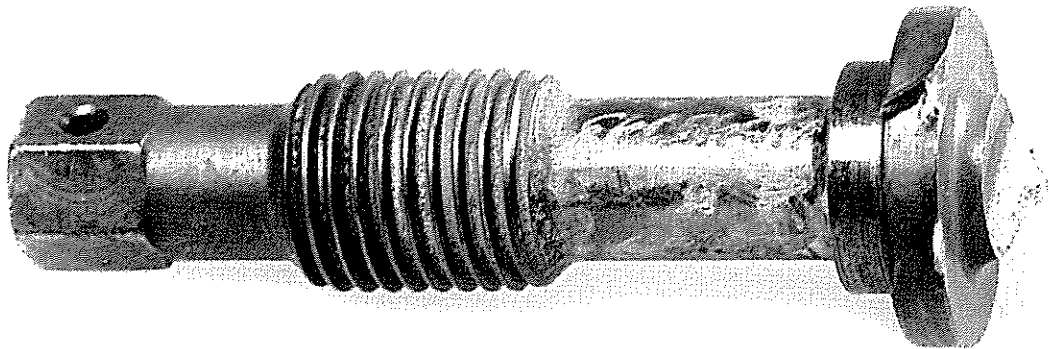


Fig. 2 Diffuser case and details of one air supply tube expansion sleeve and manifold support rod (8 o'clock position relative to the DOF)





a) Full-size sketch of an air supply manifold support rod



b) Broken rod end from the incident engine

*Fig. 3 Sketch of an air supply manifold support rod and the broken rod end from the incident engine*



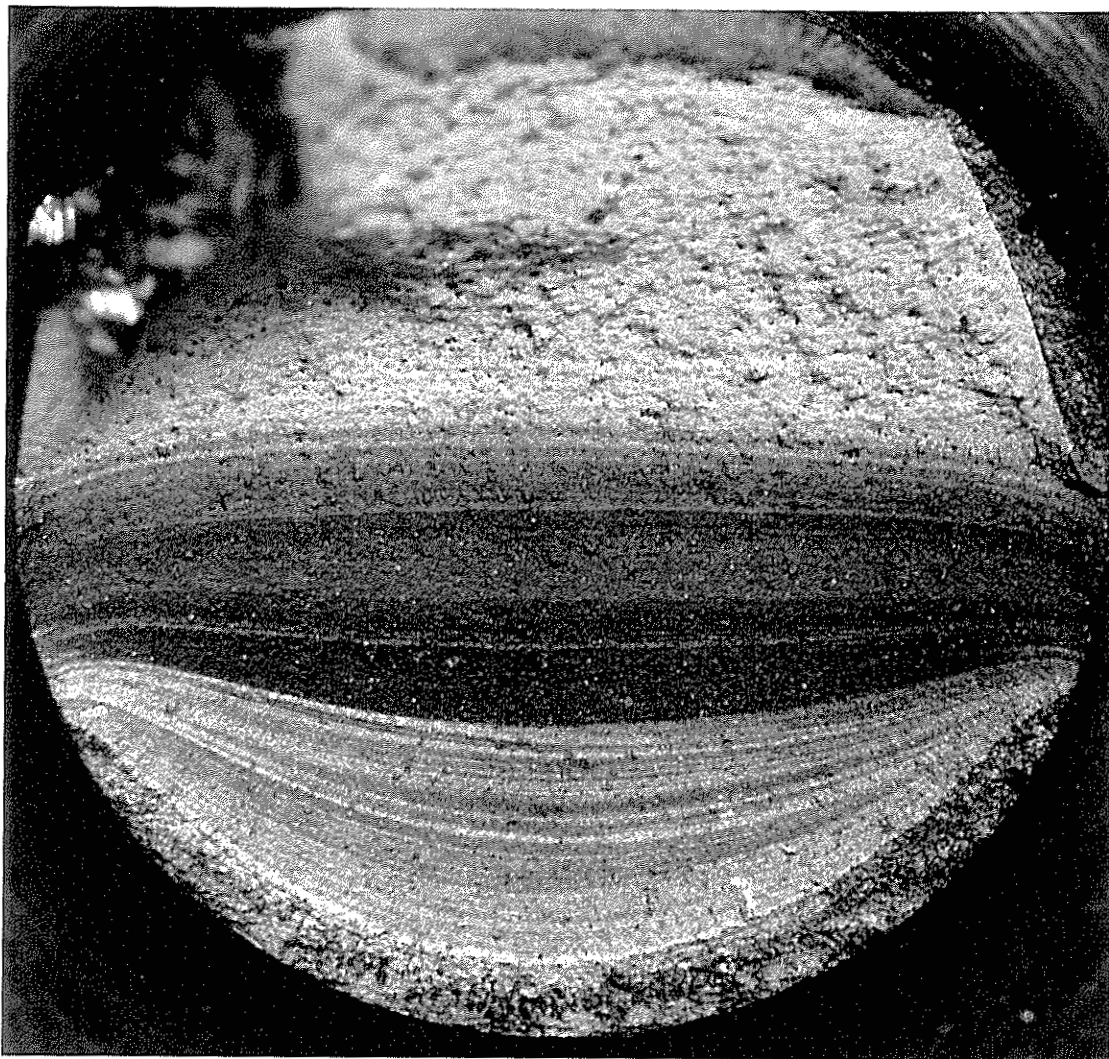


*Fig. 4 Macro photograph of the as-received fracture surface of the broken rod end.  
Magnification x18*



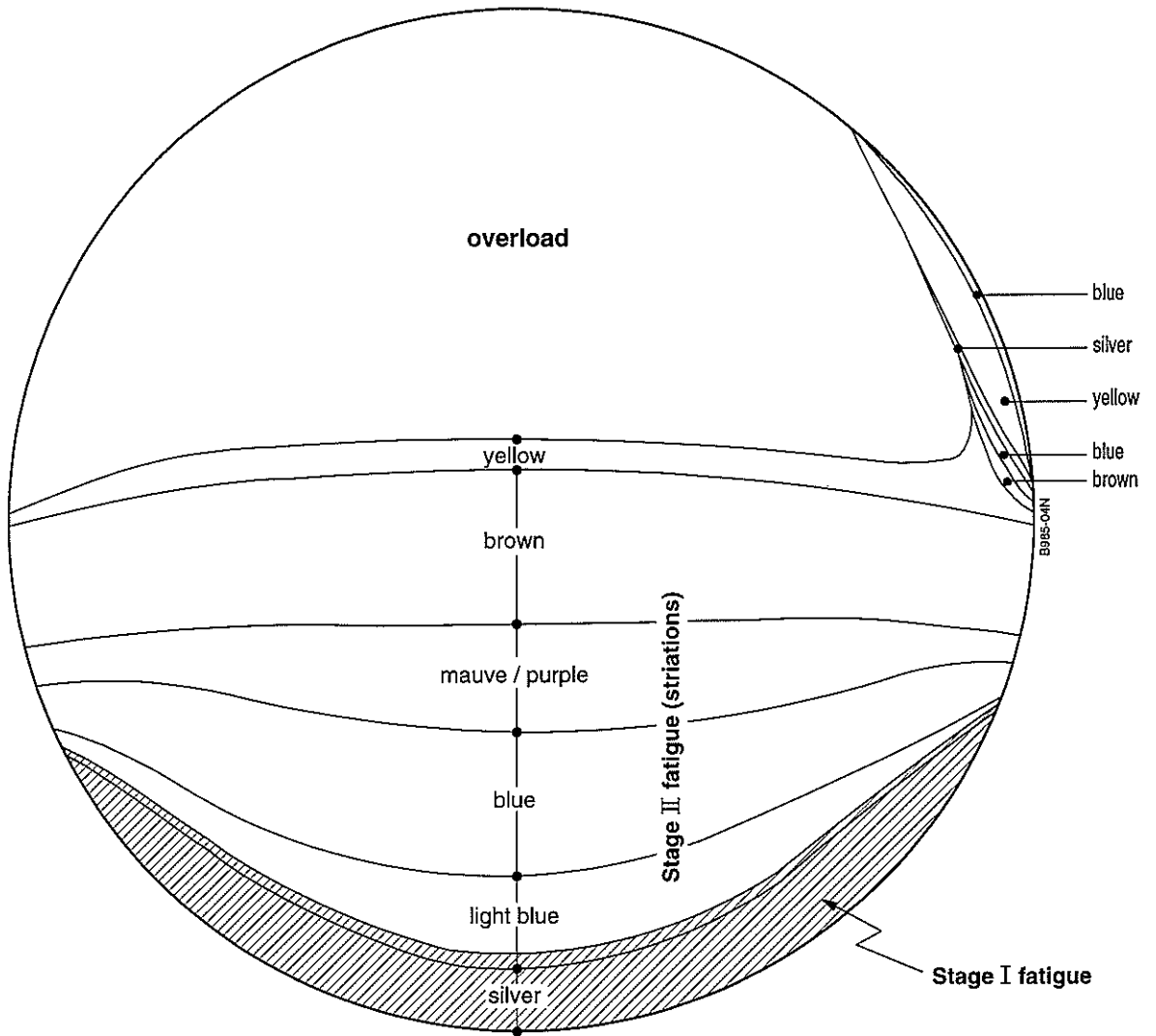
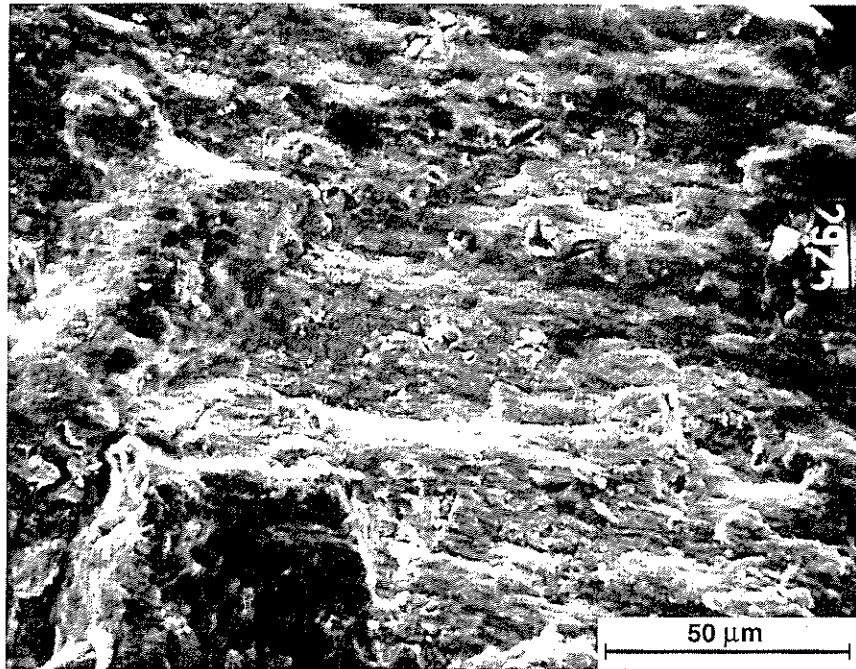
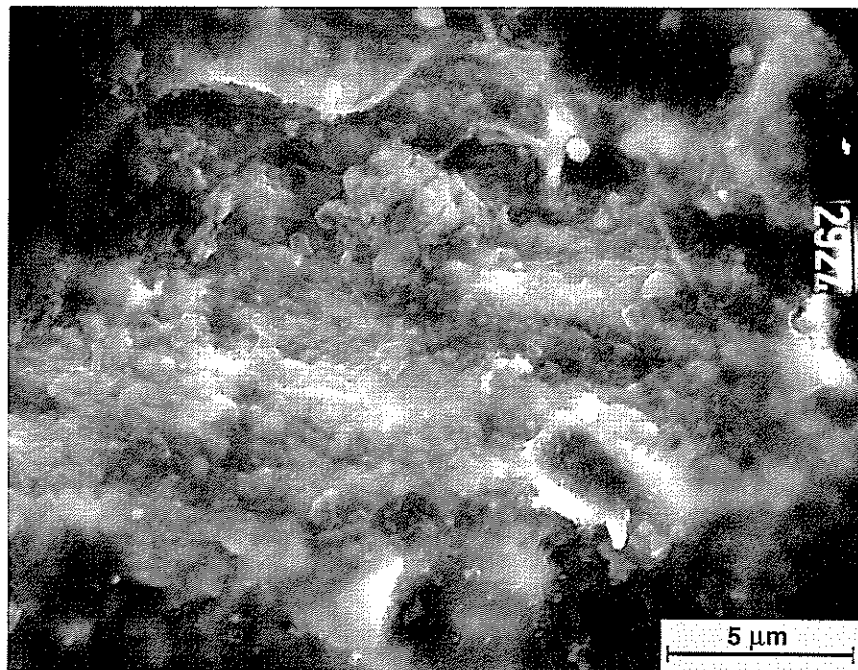


Fig. 5 Schematic of the fracture surface of the broken rod end



*Fig. 6 SEM fractograph of initiation area of the main crack in the broken rod end*



*Fig. 7 Detail of figure 6, showing severe oxidation*

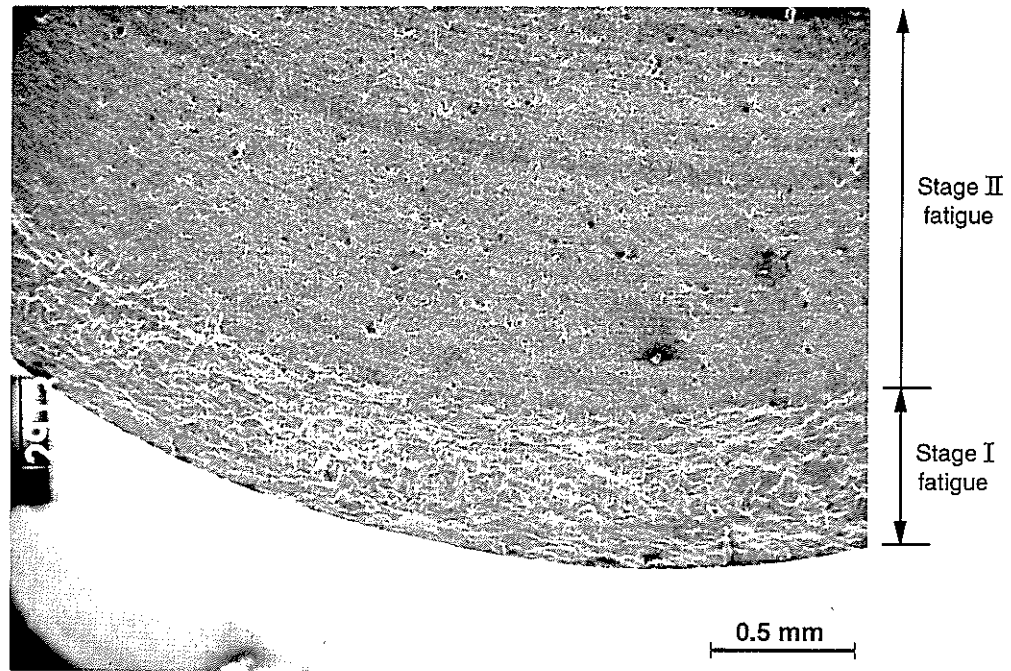


Fig. 8 SEM fractograph of Stage I → Stage II fatigue transition in the broken rod end

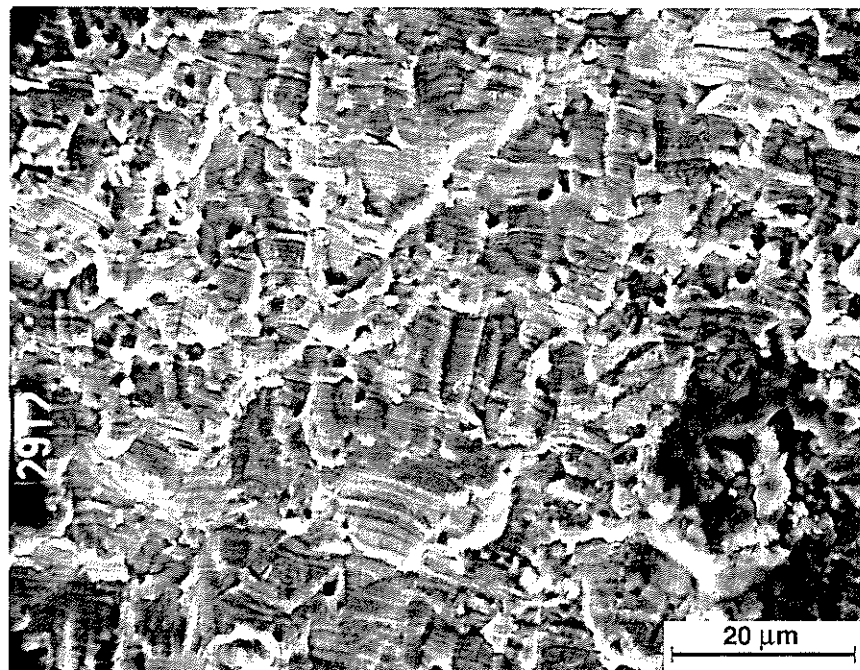
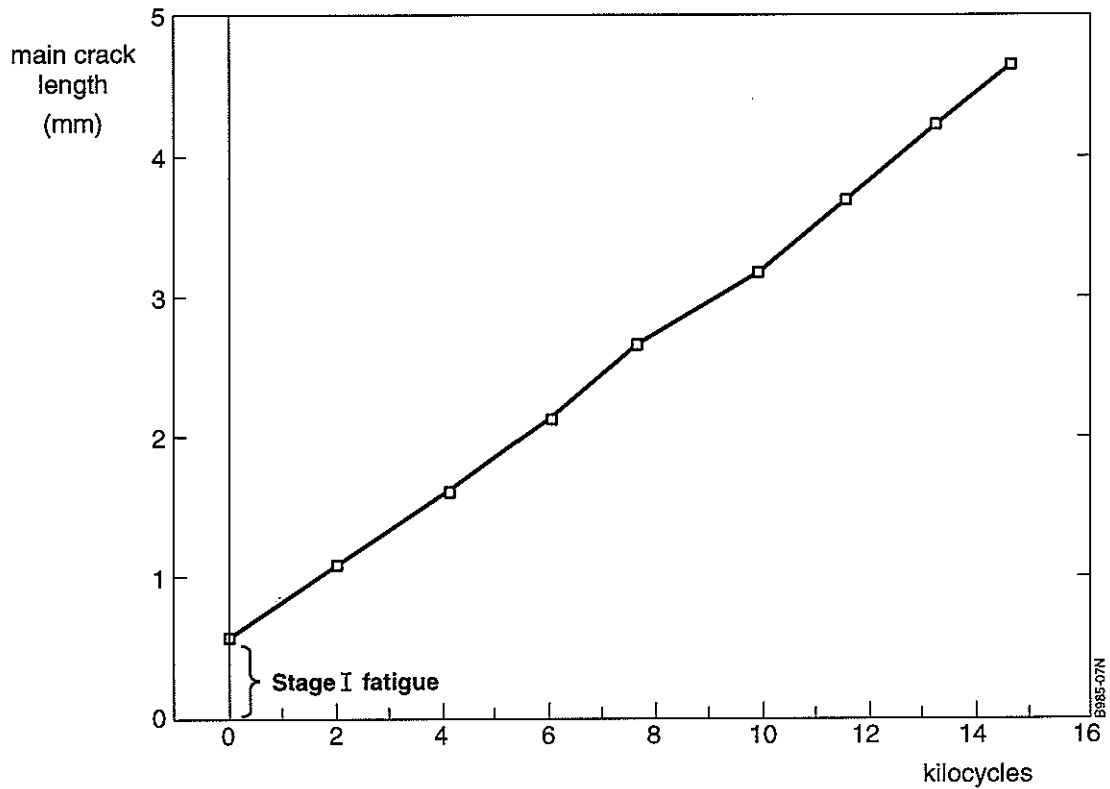


Fig. 9 Detail of figure 8 in the Stage II area, showing fatigue striations



crack depth (mm)	striation spacing (mm)	increment cycles	total cycles
0			
0.57	0.00021	0	0
1.10	0.00026	2048	2048
1.62	0.00025	2101	4149
2.14	0.00027	1902	6051
2.66	0.00033	1607	7659
3.19	0.00023	2280	9939
3.71	0.00032	1619	11559
4.23	0.00031	1663	13222
4.65	0.00030	1402	14625

Fig. 10 Striation cycle count for Stage II fatigue in the broken rod end

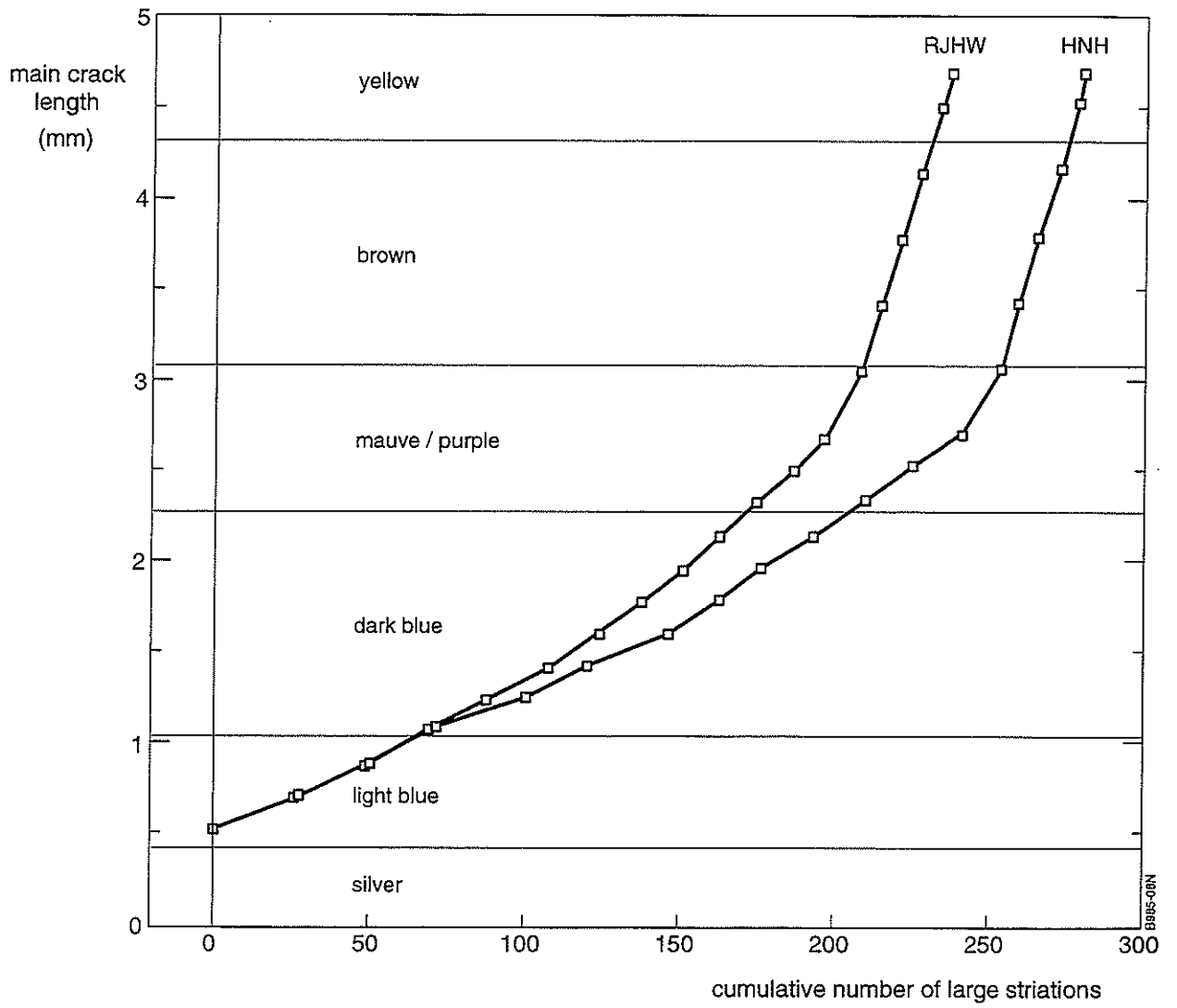


Fig. 11 Cumulative number of large striations for Stage II fatigue in the broken rod end.  
The positions of the broad divisions of interference colours are indicated as well



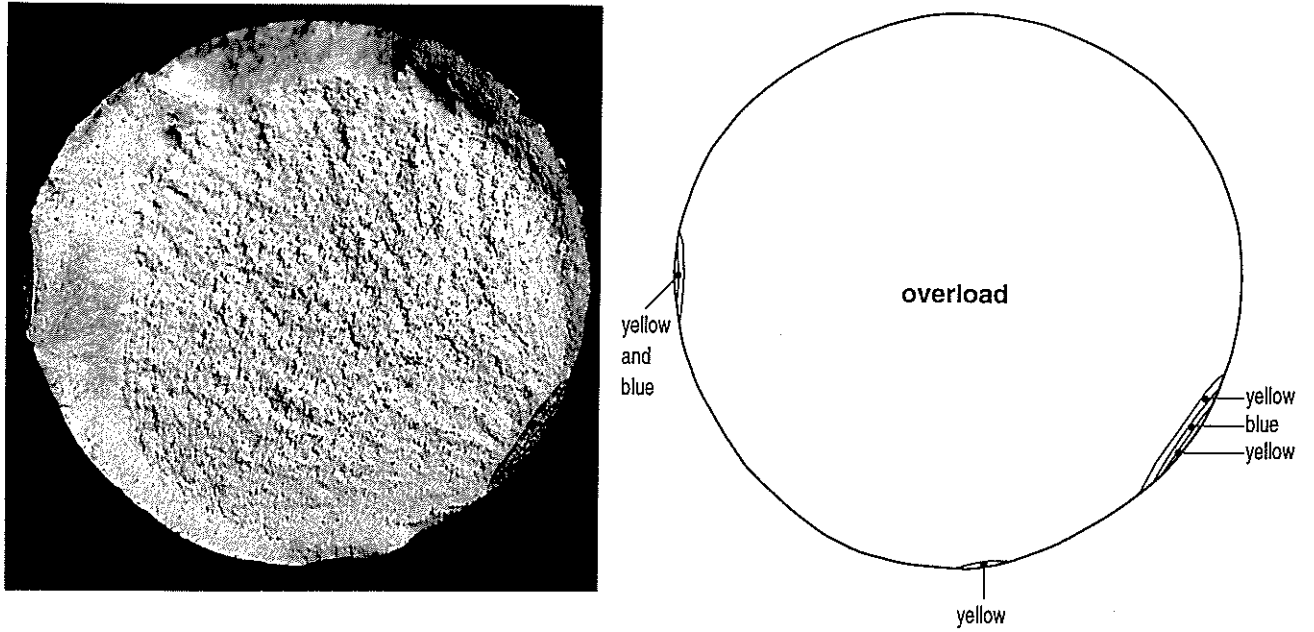


Fig. 12 Macrofractograph and schematic of the fracture surface of the broken-open spherical rod end (NLR code S) from the incident engine

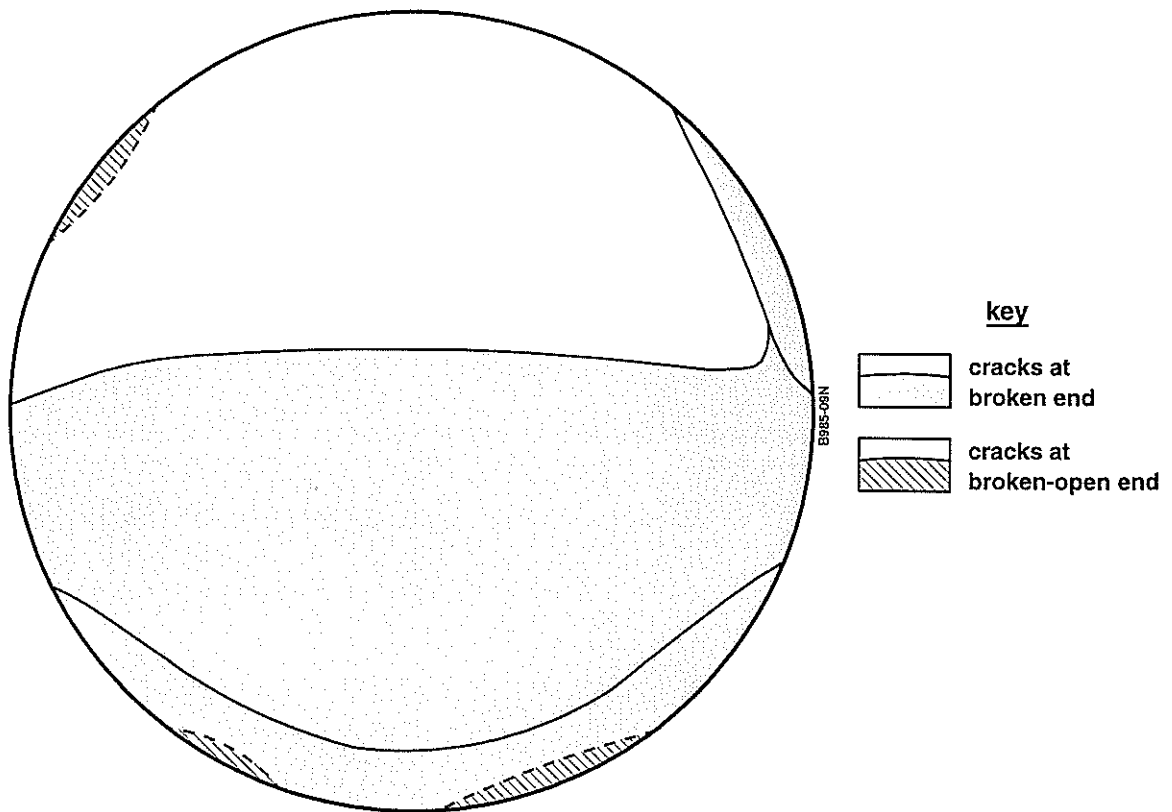


Fig. 13 Relative positions, viewed in the outboard direction, of the cracks in the broken/broken-open rod (NLR code S) from the incident engine



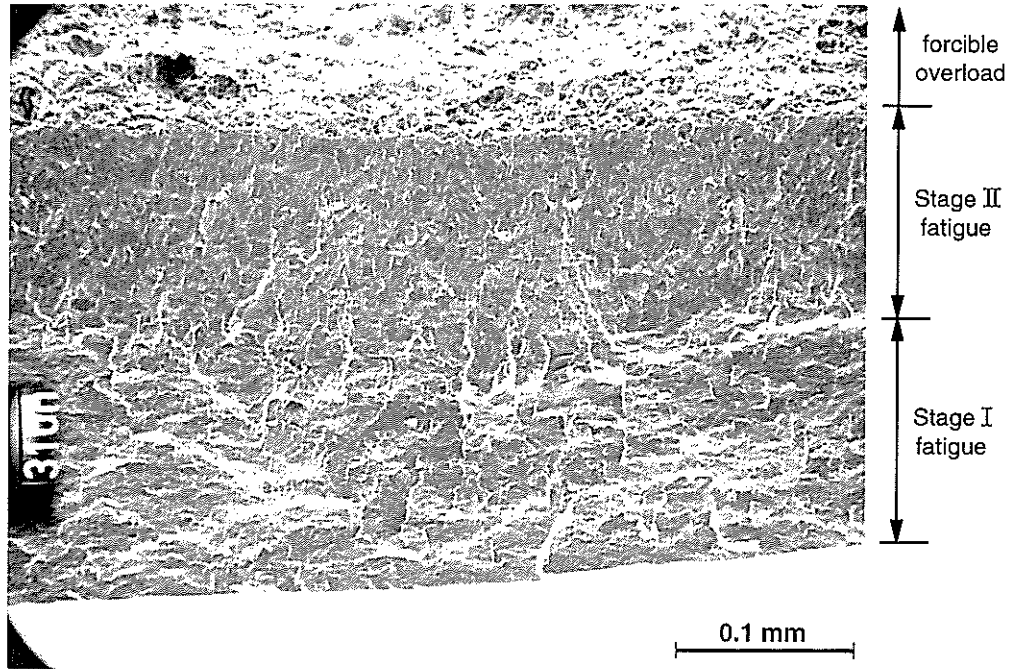


Fig. 14 SEM fractograph of Stage I → Stage II fatigue transition in the broken-open spherical rod end (NLR code S) from the incident engine

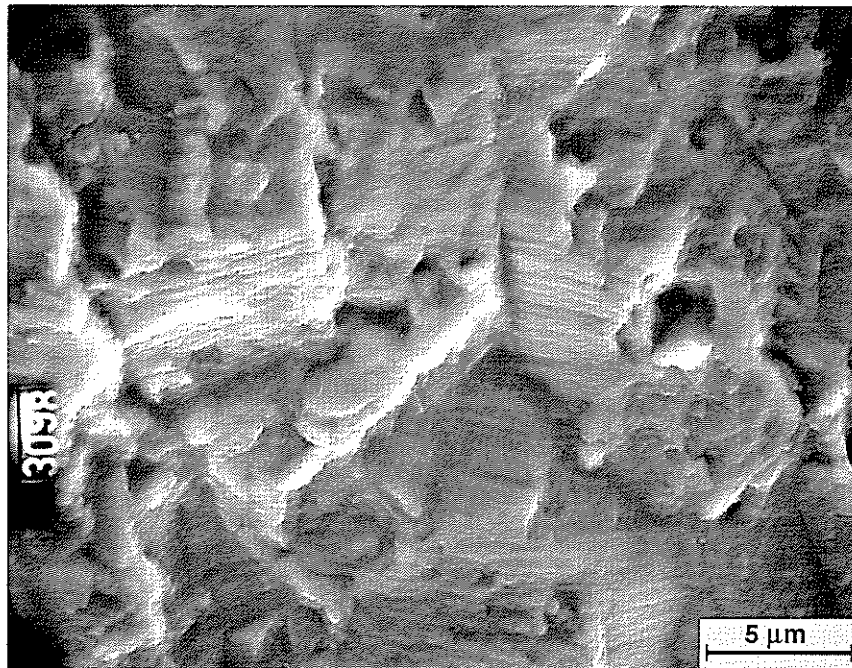


Fig. 15 Detail of figure 14 in the Stage II area just beyond Stage I



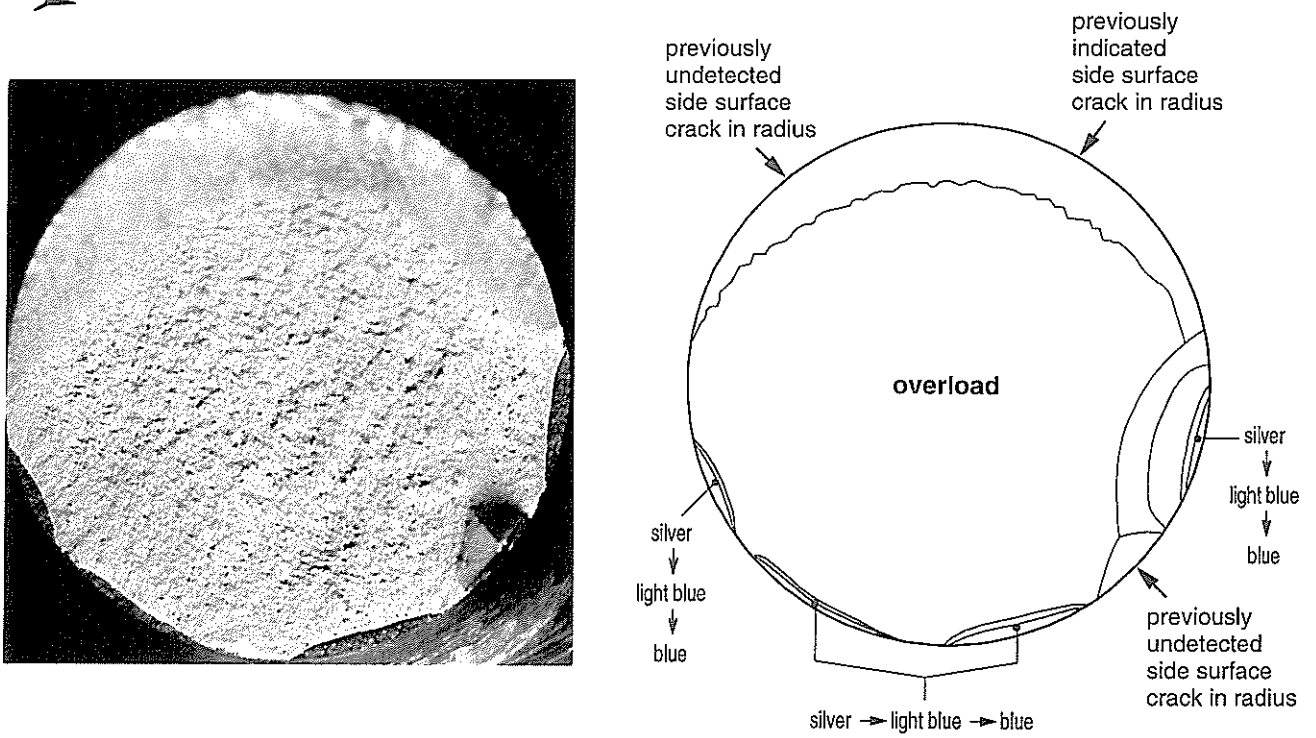


Fig. 16 Macrofractograph and schematic of the fracture surface of the broken-open rod (NLR code  $S_1$ ) from the incident engine

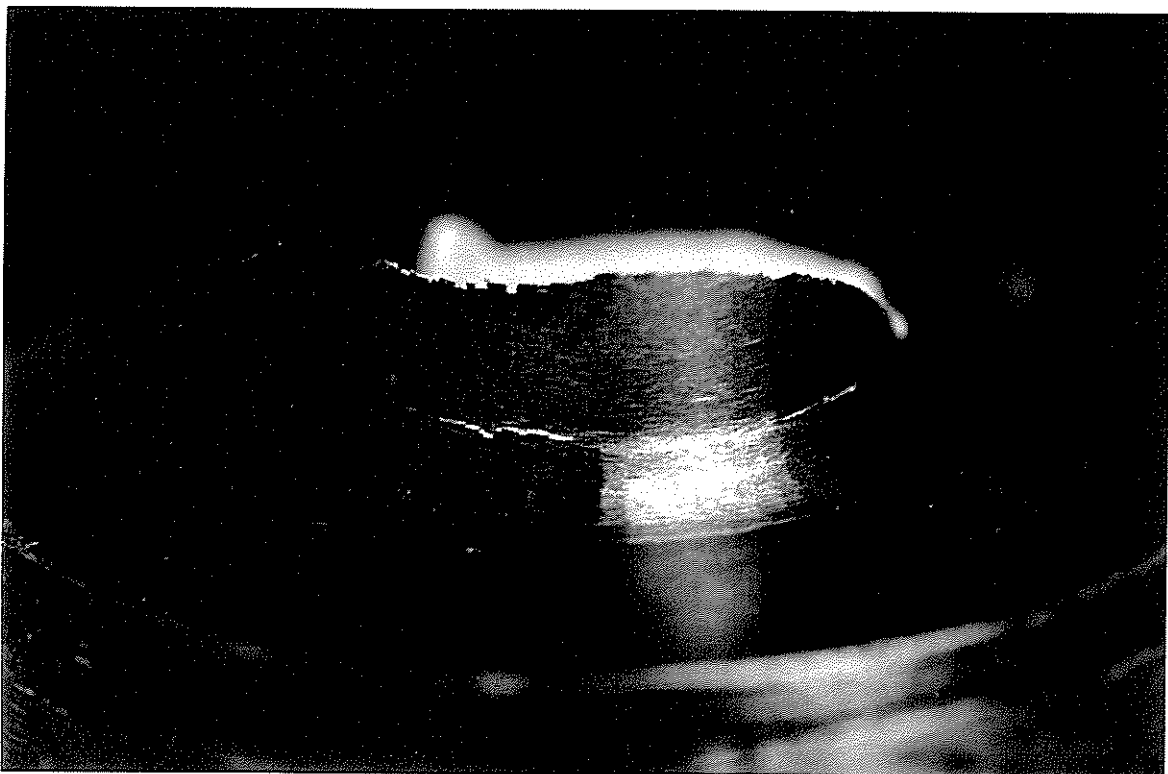


Fig. 17 Two of the partly opened cracks in the broken-open rod (NLR code  $S_1$ ) from the incident engine



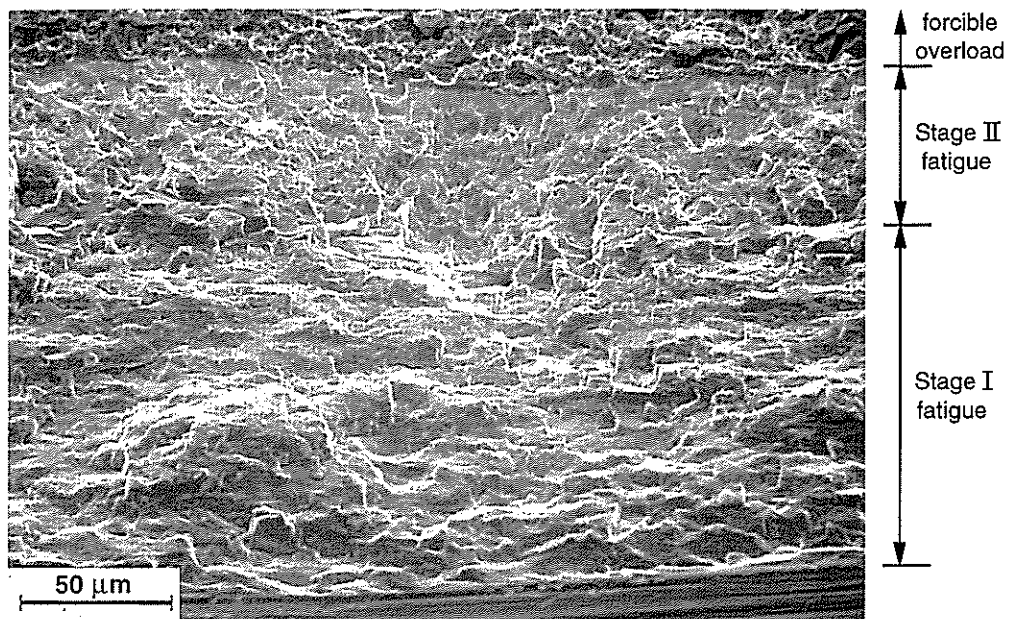


Fig. 18 SEM fractograph of Stage I → Stage II fatigue transition in the broken-open spherical rod end (NLR code S<sub>1</sub>) from the incident engine

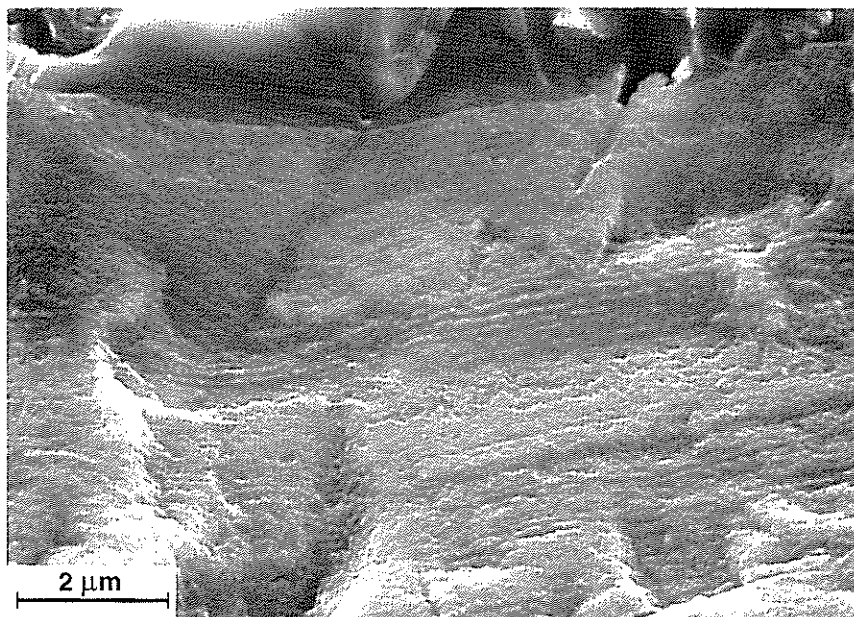


Fig. 19 Much-oxidised fatigue striations for one of the cracks in the broken-open spherical rod end (NLR code S<sub>1</sub>) from the incident engine



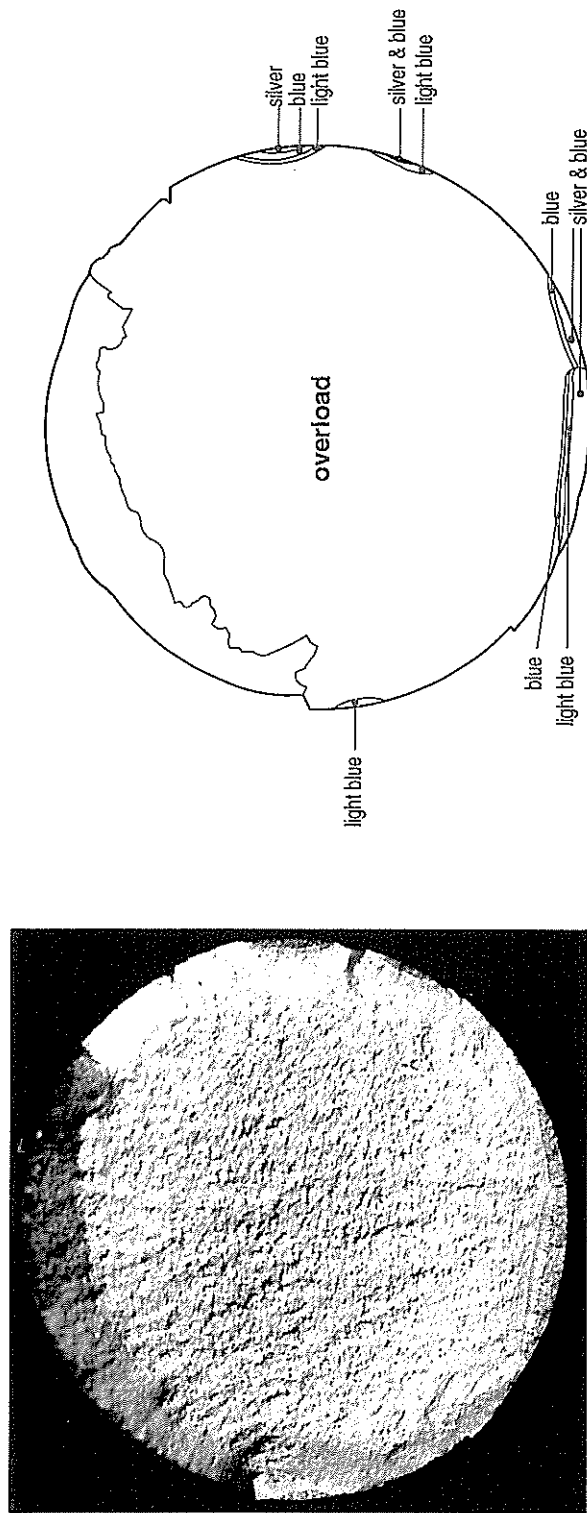


Fig. 20 Macrofractograph and schematic of the fracture surface of a broken-open rod (NLR code A)



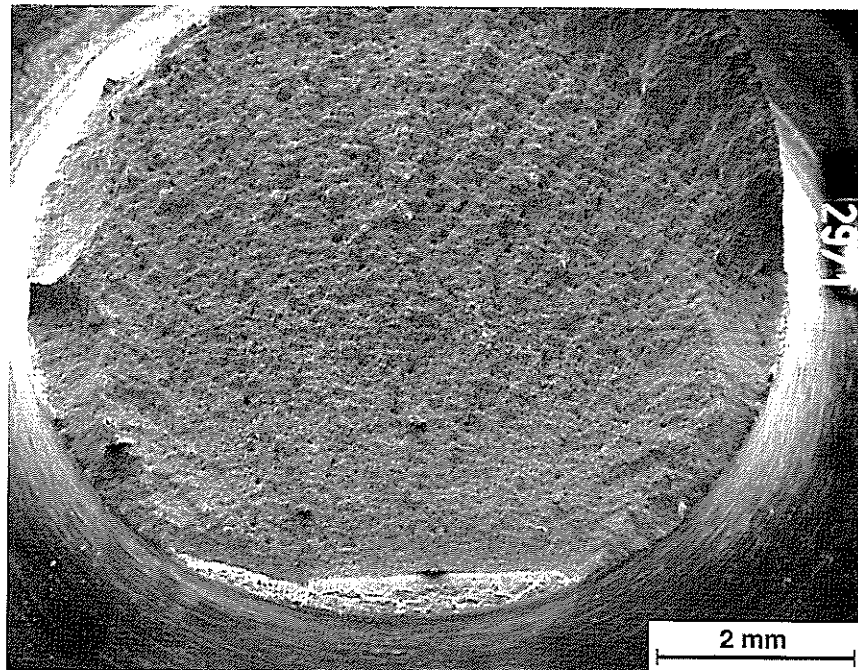


Fig. 21 Low magnification SEM fractograph of a broken-open spherical rod end (NLR code A); see also figure 20, which shows the mating fracture surface

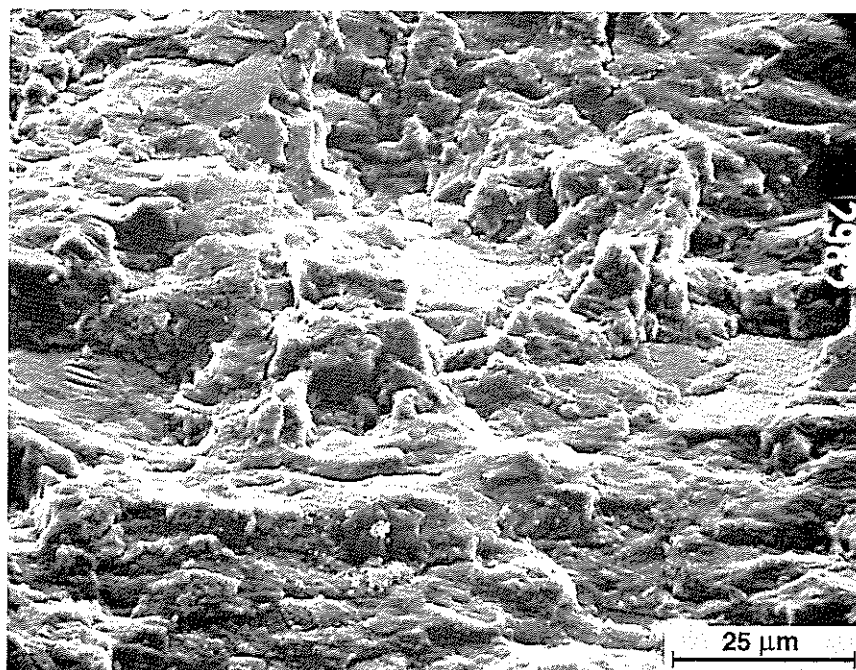


Fig. 22 Detail of initiation area of main crack in figure 21, showing severe oxidation

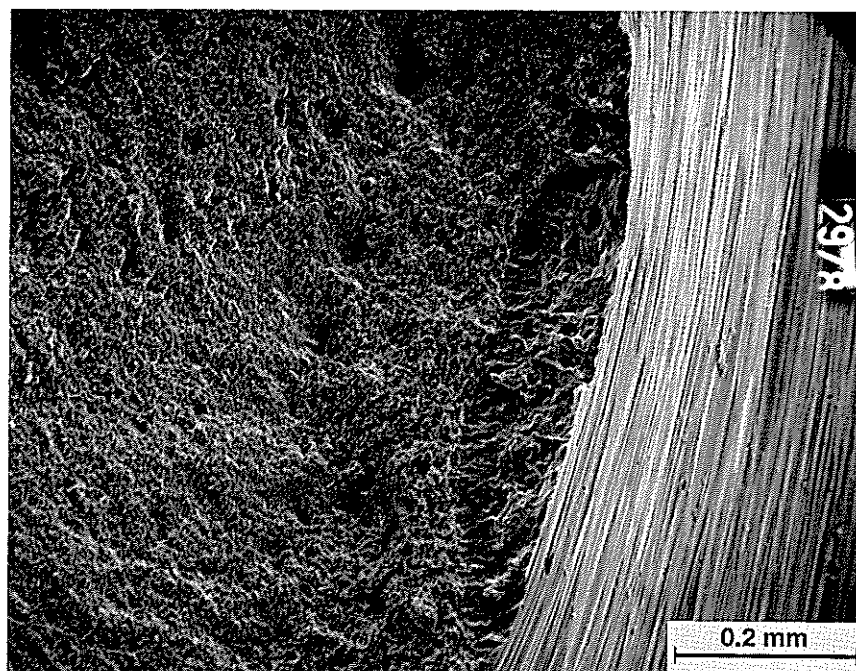


Fig. 23 SEM fractograph of crack at 3 o'clock position in figure 21

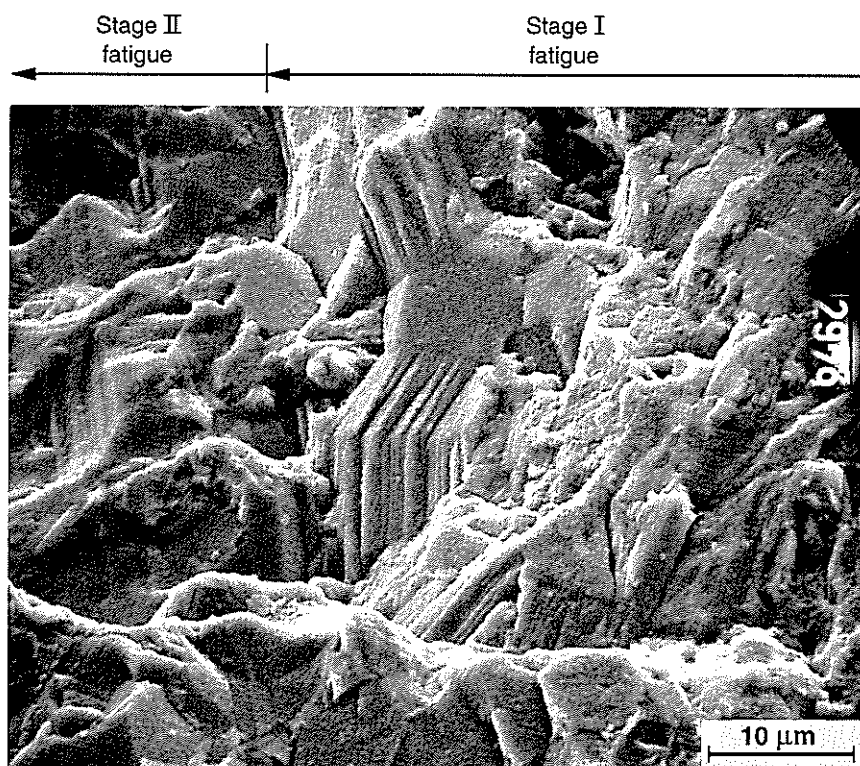
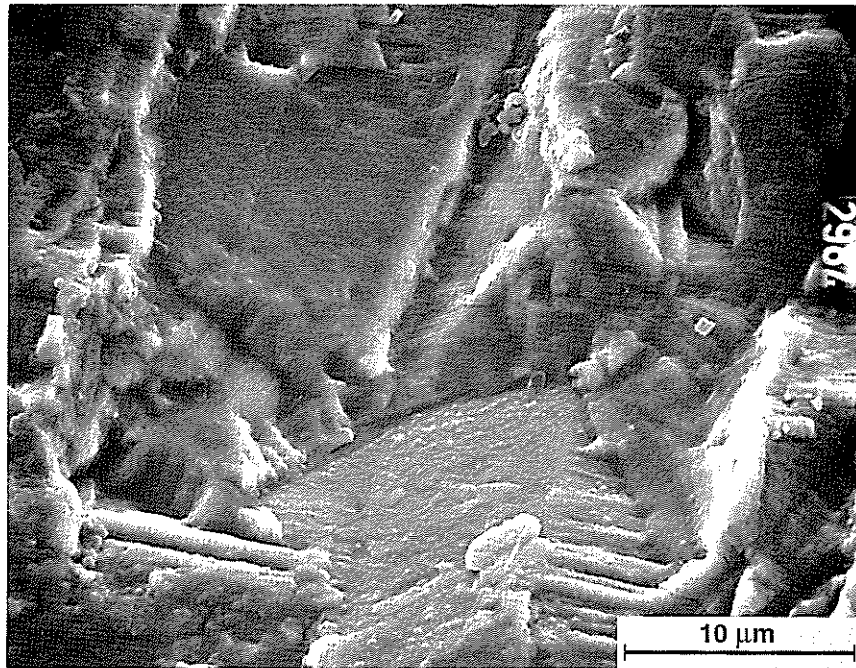
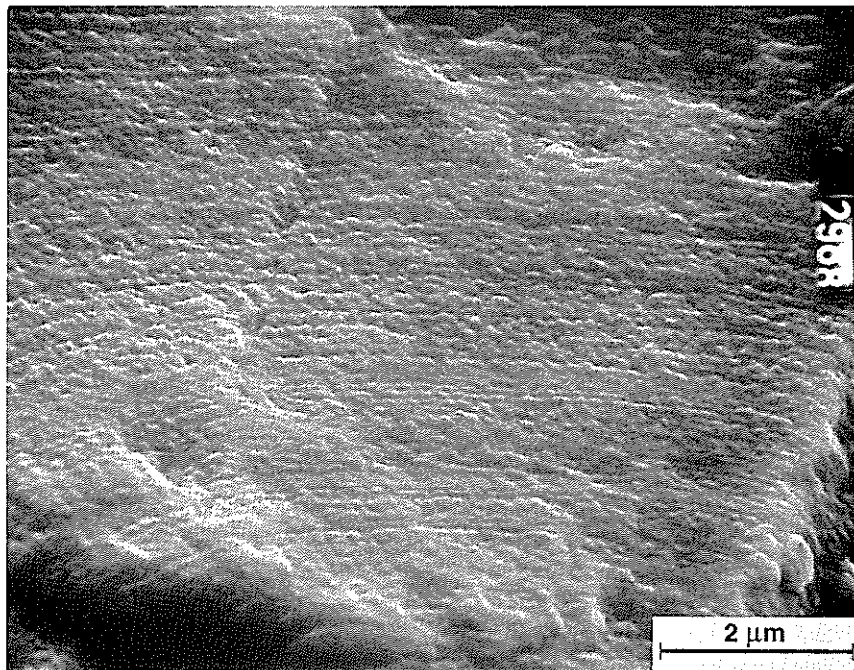


Fig. 24 Detail of figure 23, showing Stage I → Stage II fatigue transition



a) Stage I  $\rightarrow$  Stage II transition,  $0^\circ$  tilt



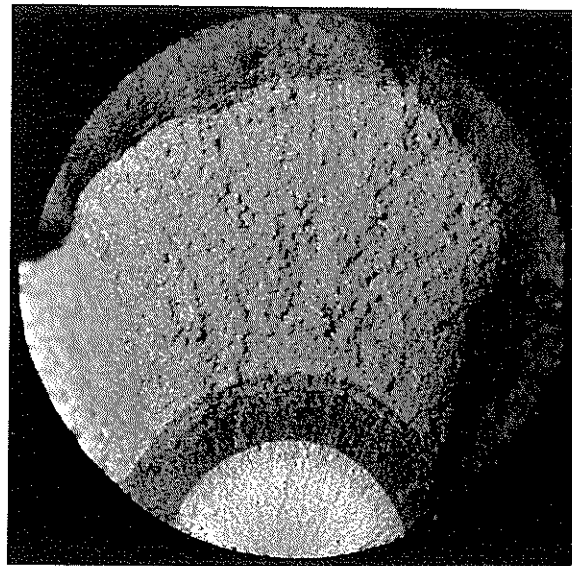
b) Detail of (a) above,  $20^\circ$  tilt

*Fig. 25 Fatigue striations at the beginning of Stage II fatigue for the crack at the 6 o'clock position in figures 20 and 21*

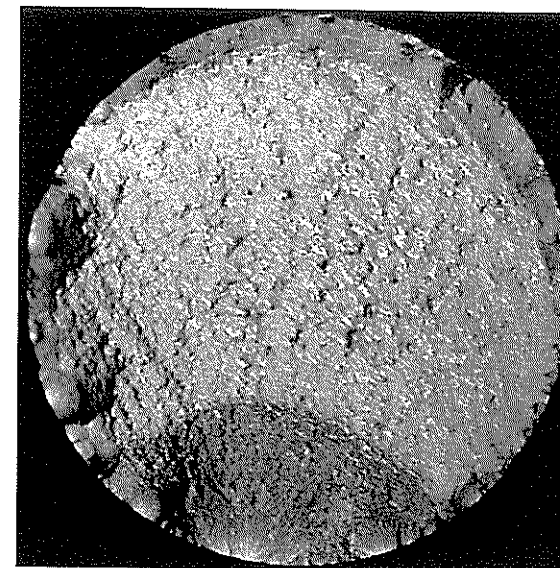




**Specimen LTF 56**  
 R = -0.5, trapezoidal waveform,  
 0.25 Hz,  $\sigma_{\max} = 812$  MPa  
 $N_f = 43,363$  cycles  
 time to failure = 48.2 hours



**Specimen LTF 110**  
 HOT TURBISTAN, R = -0.5,  
 $\sigma_{\max} = 900$  MPa  
 $N_f = 8000$  flights  
 time to failure = 640 hours



**Specimen LTF 53**  
 R = -1.0, trapezoidal waveform,  
 0.25 Hz,  $\sigma_{\max} = 770$  MPa  
 $N_f = 2655$  cycles  
 time to failure = 2.95 hours

*Fig. 26 Shapes and interference colours for low-cycle fatigue cracks produced by tension - compression loading of cylindrical specimens of Inconel 718 at 600° C. These specimens were tested as part of the NLR's contribution to the IEPG TA 31 programme*



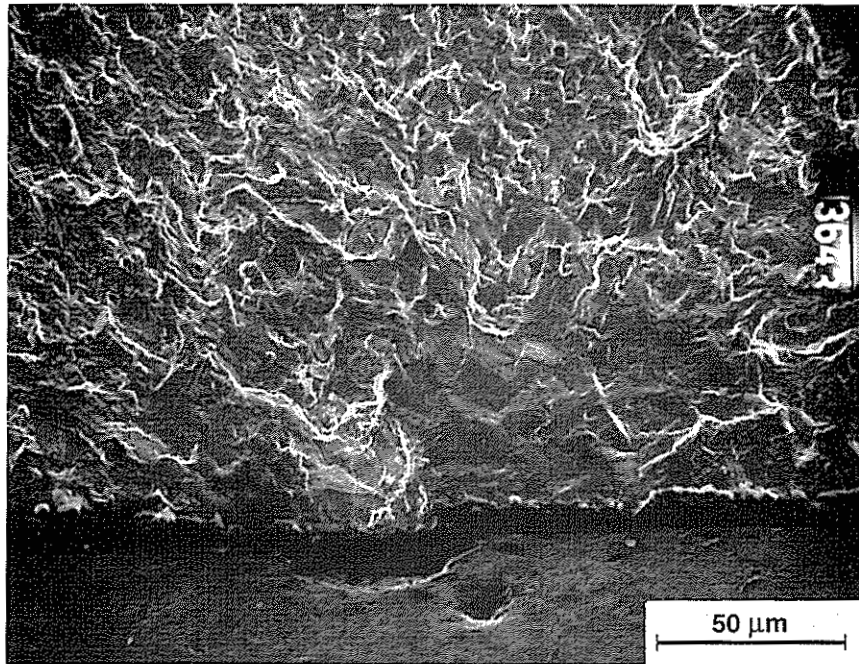


Fig. 27 SEM fractograph of initiation area of the fatigue crack in specimen LTF 110

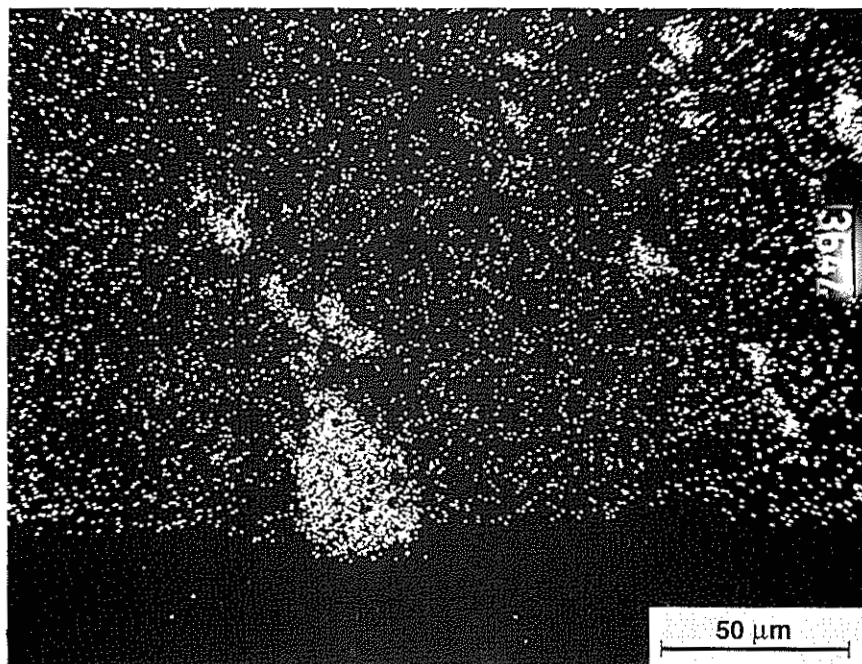


Fig. 28 EDX mapping of the same area in figure 27, showing that fatigue initiated at a large NbC particle

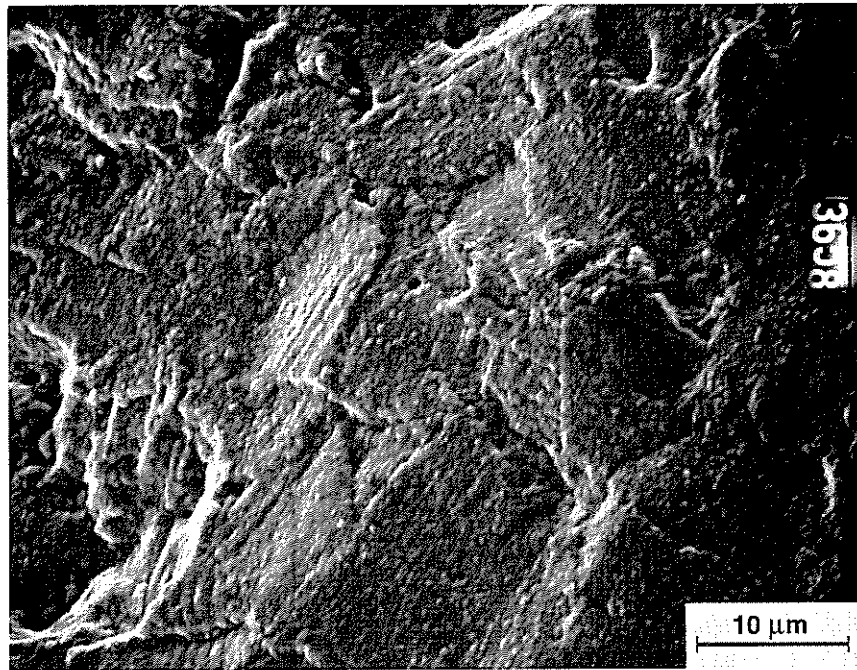


Fig. 29 Detail of figure 27, showing severely oxidised Stage I fatigue

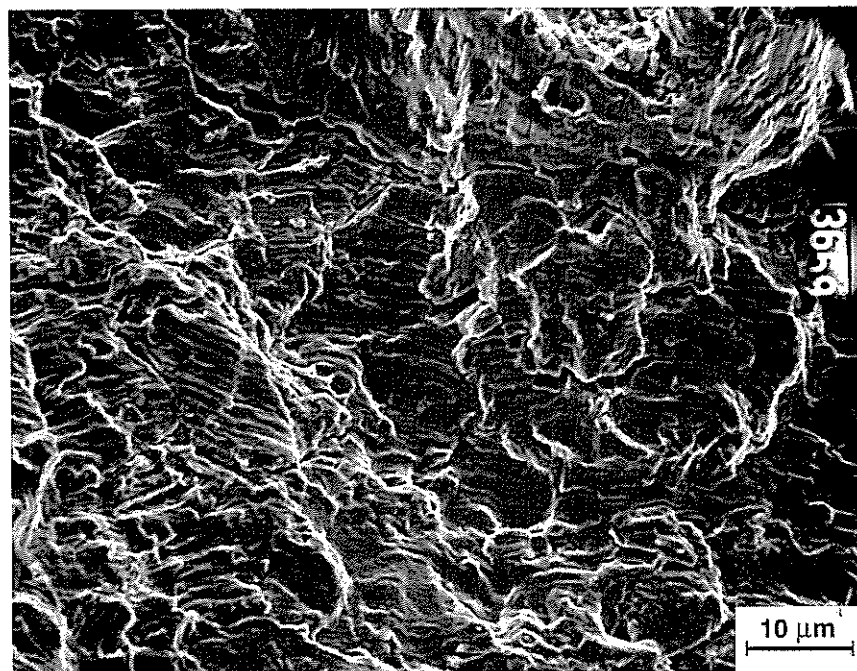
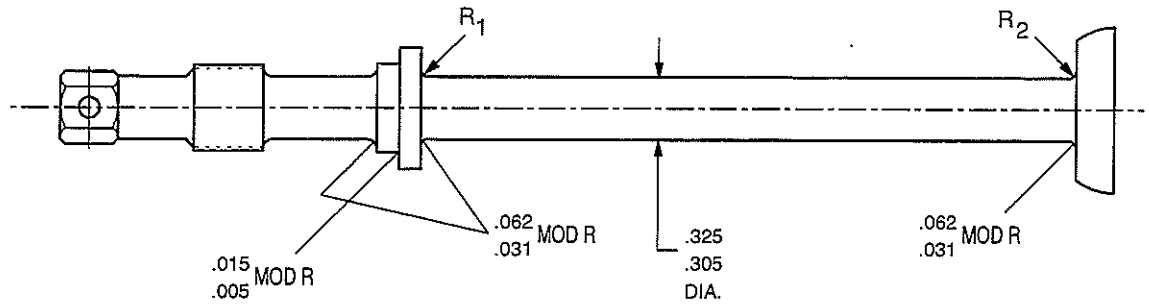


Fig. 30 Detail of the Stage II fatigue fracture surface of specimen LTF 110, showing fatigue striations



a) Specification mod radii: dimensions in inches

Rod codes		Remarks	R <sub>1</sub> (in.)	R <sub>2</sub> (in.)
NLR	MFG date code			
S	59	broken, incident engine	0.062	0.061
S <sub>1</sub>	59	broken-open, incident engine	0.069	0.067
A	59	broken-open	0.055	0.063
B	59		0.054	0.049
C	67		0.050	0.051
D	67		0.042	0.051
E	123		0.065	0.053
F	129	new rod	0.062	0.035
G	39		0.061	0.069
H	39		0.060	0.055

BB85-20N

b) Average measured values of radii R<sub>1</sub> and R<sub>2</sub>

Fig. 31 Profile projector average values of mod radii R<sub>1</sub> and R<sub>2</sub>

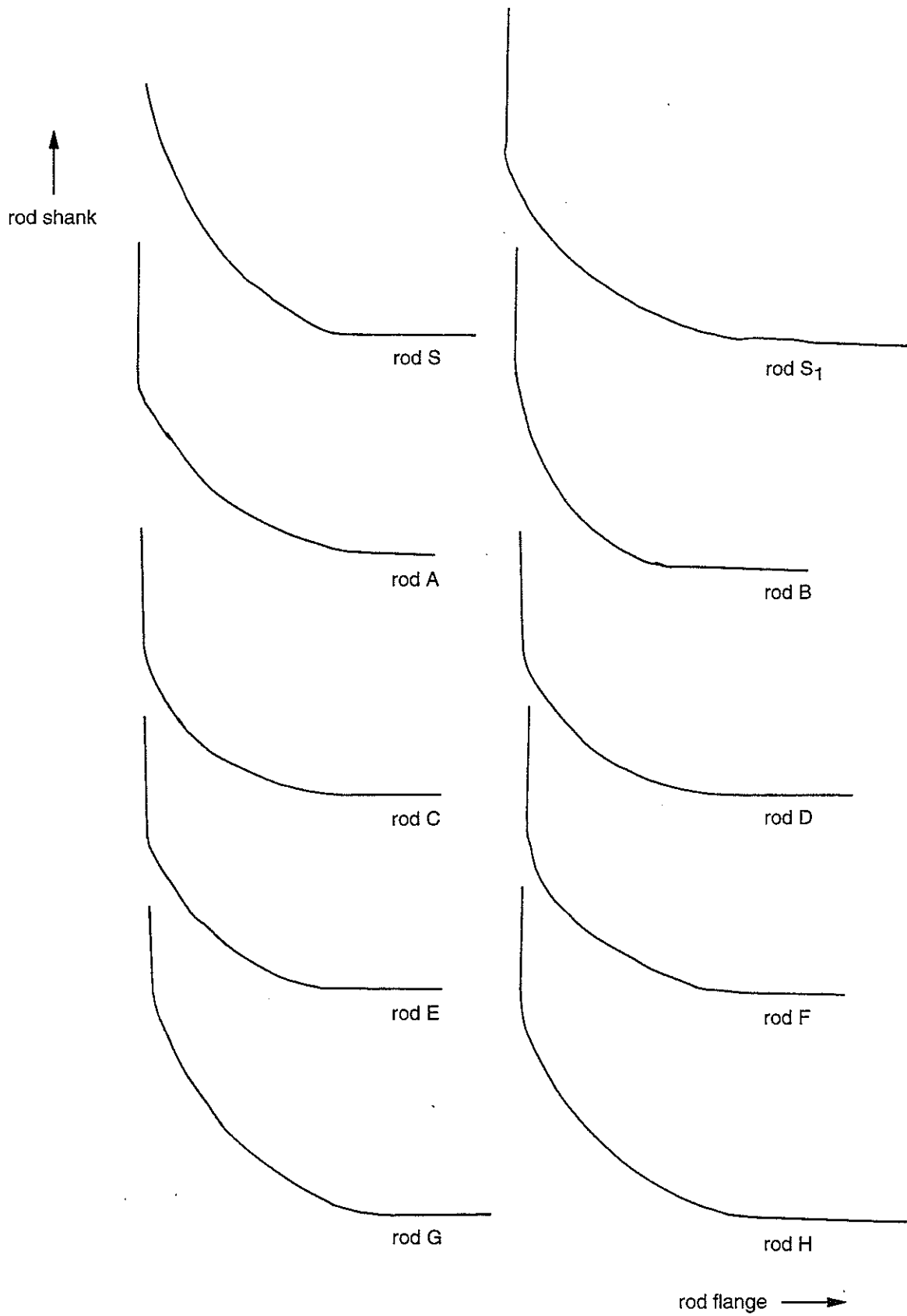


Fig. 32 Mod radius  $R_1$  profiles

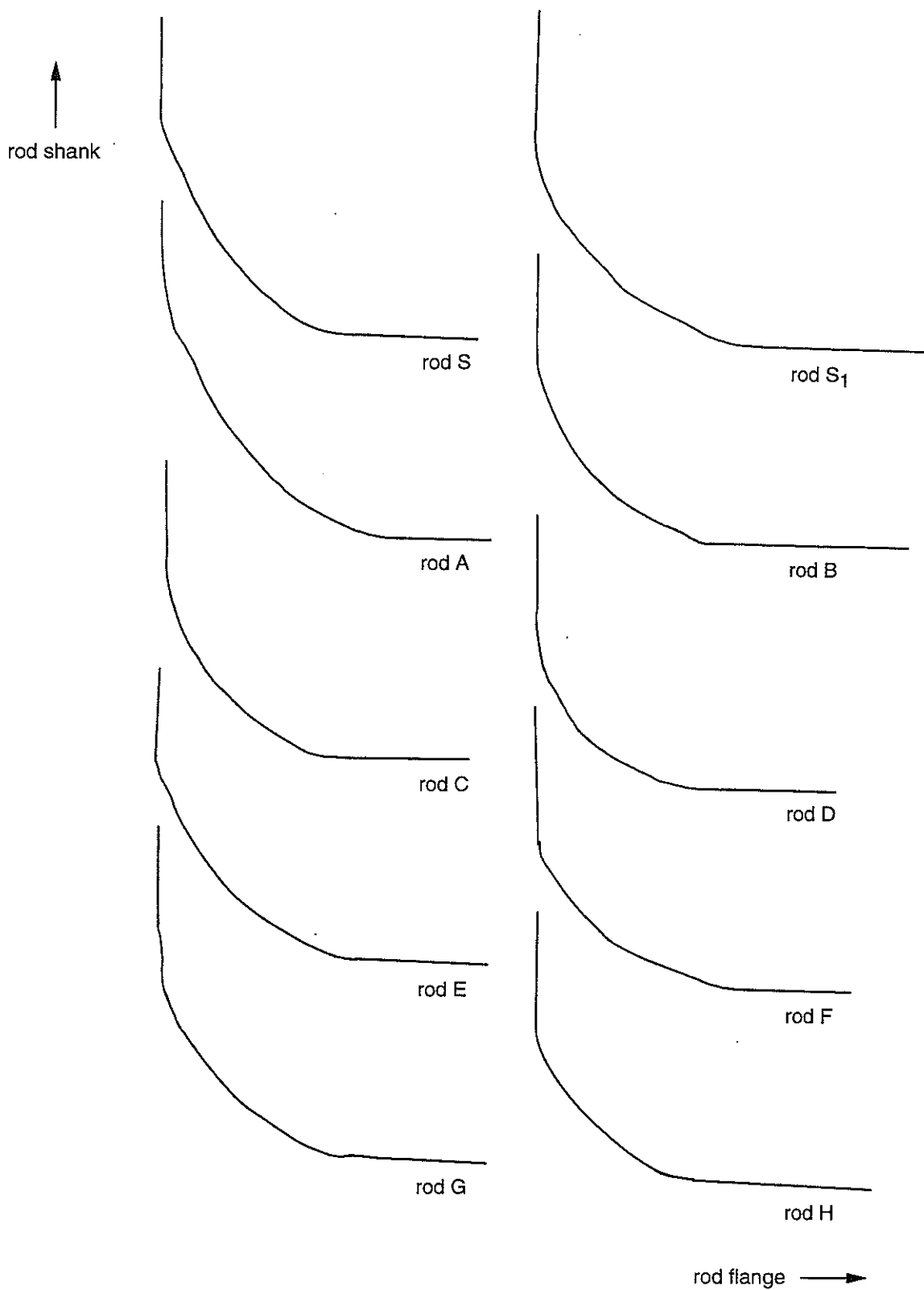
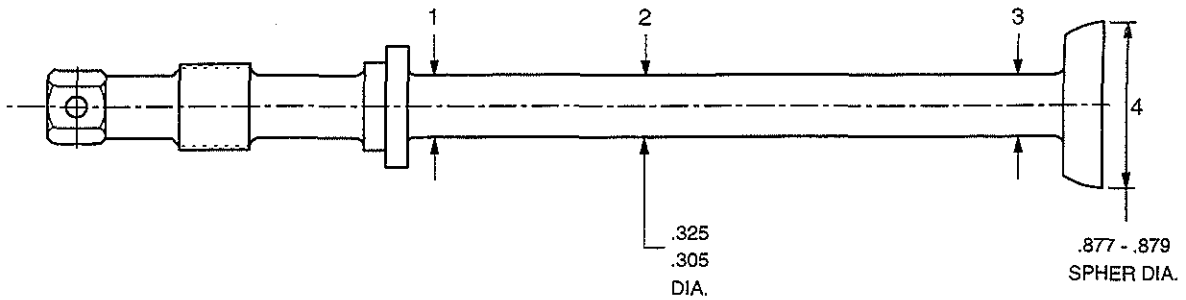


Fig. 33 Mod radius  $R_2$  profiles



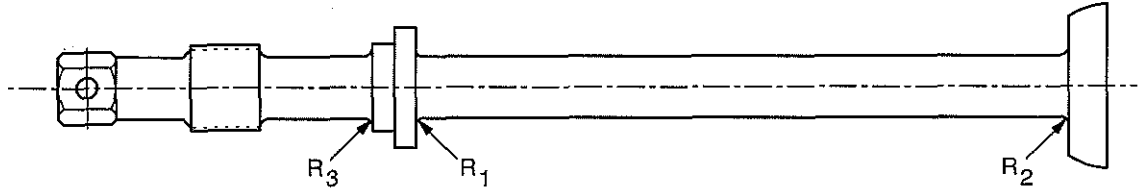
a) Locations of diameter measurements: dimensions in inches

Rod codes		Remarks	Measurements locations			
NLR	MFG date code		1 (in.)	2 (in.)	3 (in.)	4 (in.)
S	59	broken, incident engine	0.316	0.319	0.319	0.878
S <sub>1</sub>	59	broken-open, incident engine	0.317	0.319	0.318	0.878
A	59	broken-open	0.318	0.319	0.318	0.878
B	59		0.318	0.318	0.319	—
C	67		0.317	0.319	0.318	—
D	67		0.317	0.319	0.318	0.877
E	123		0.318	0.318	0.318	—
F	129	new rod	0.318	0.320	0.318	0.877
G	39		0.313	0.315	0.316	0.878
H	39		0.315	0.316	0.315	0.877

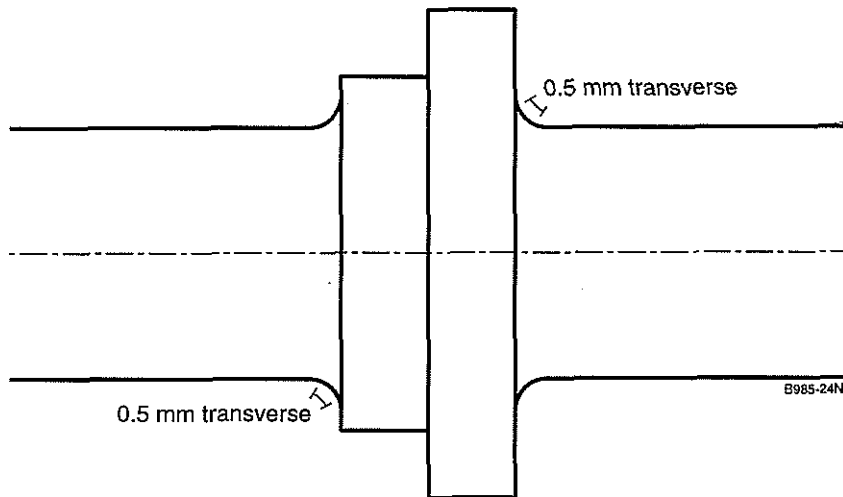
B995-23N

b) Measured diameters

Fig. 34 Diameter measurements of rods



a) Locations of the surface roughness measurements



b) Sketch to illustrate the measurement of roughness in a radius

Fig. 35 Illustrations of how surface roughness measurements were made for several air supply manifold support rods

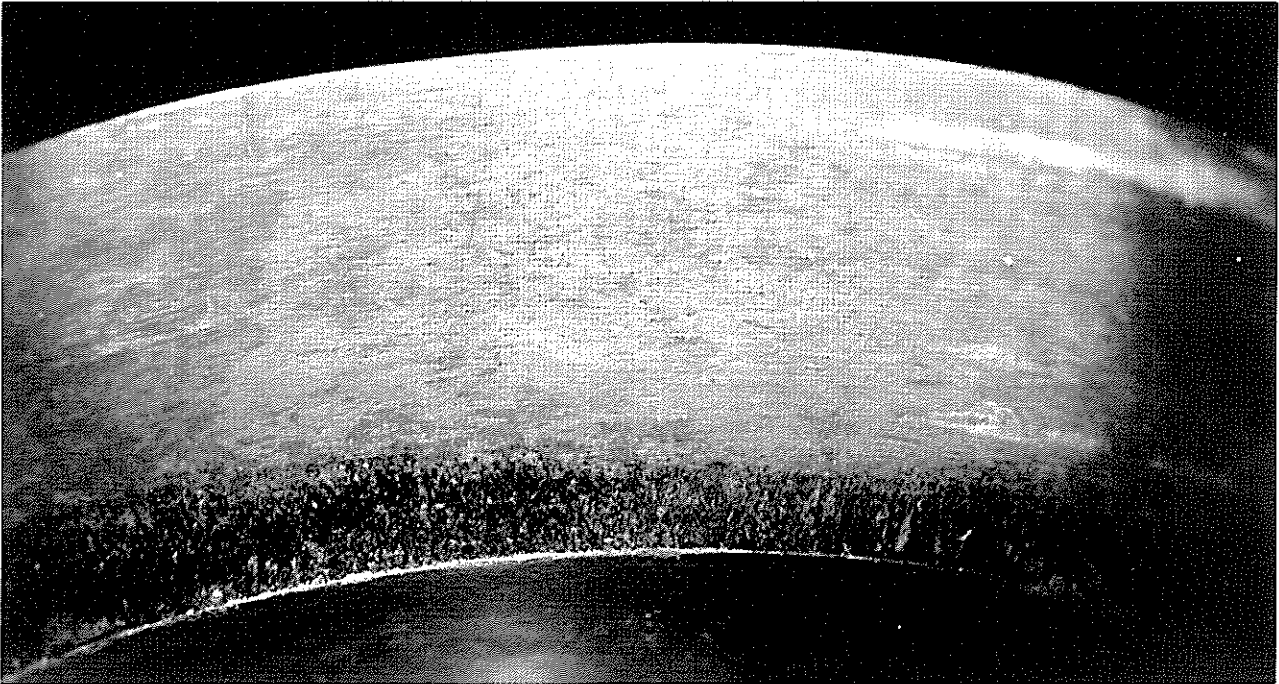


Fig. 36 Local fretting on the spherical rod end of the broken rod from the incident engine (NLR code S)

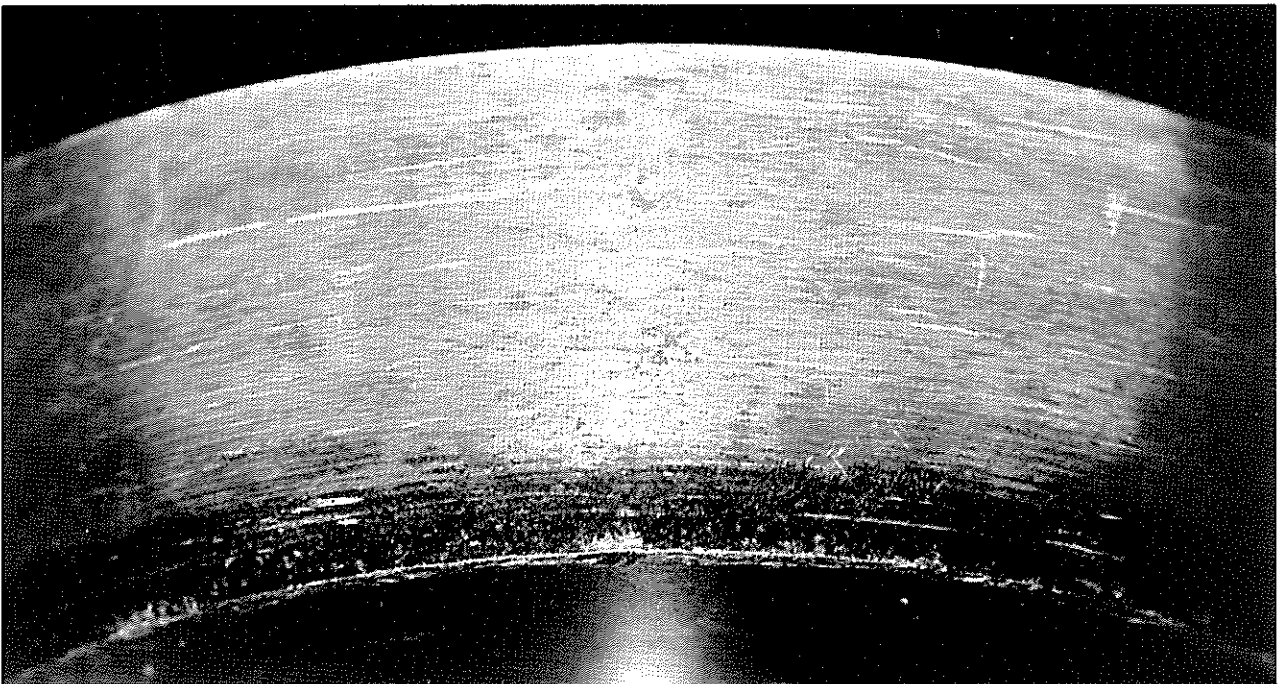
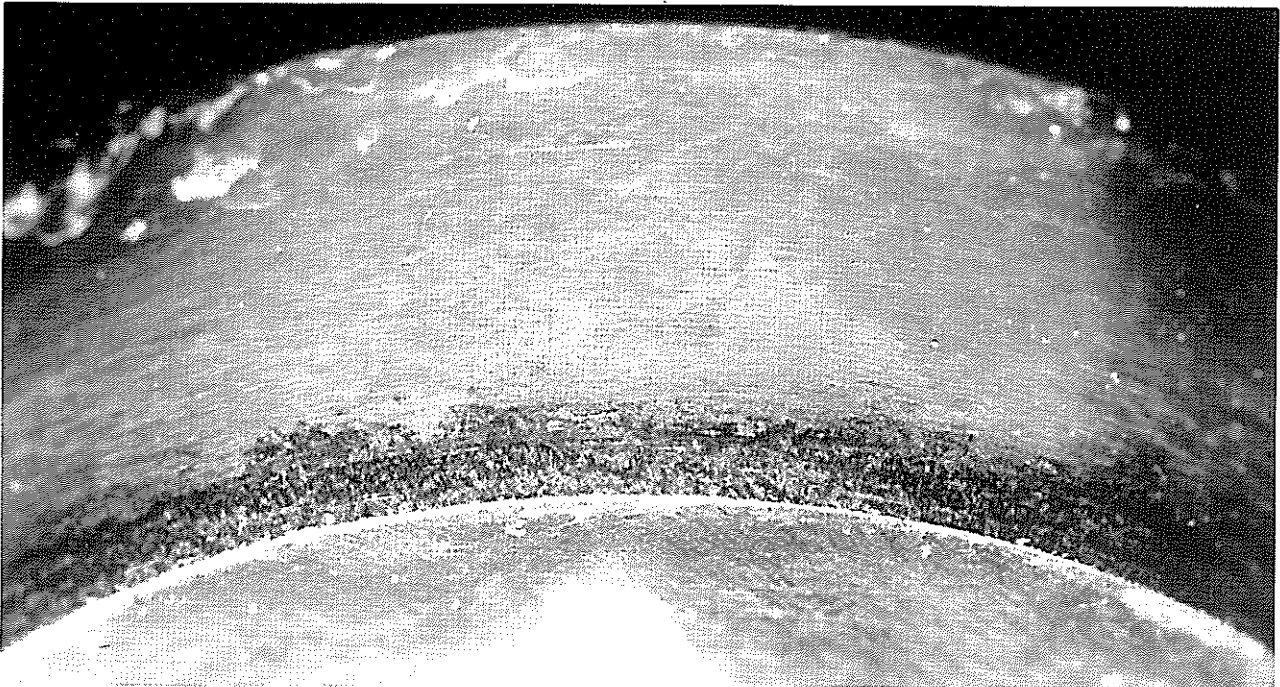
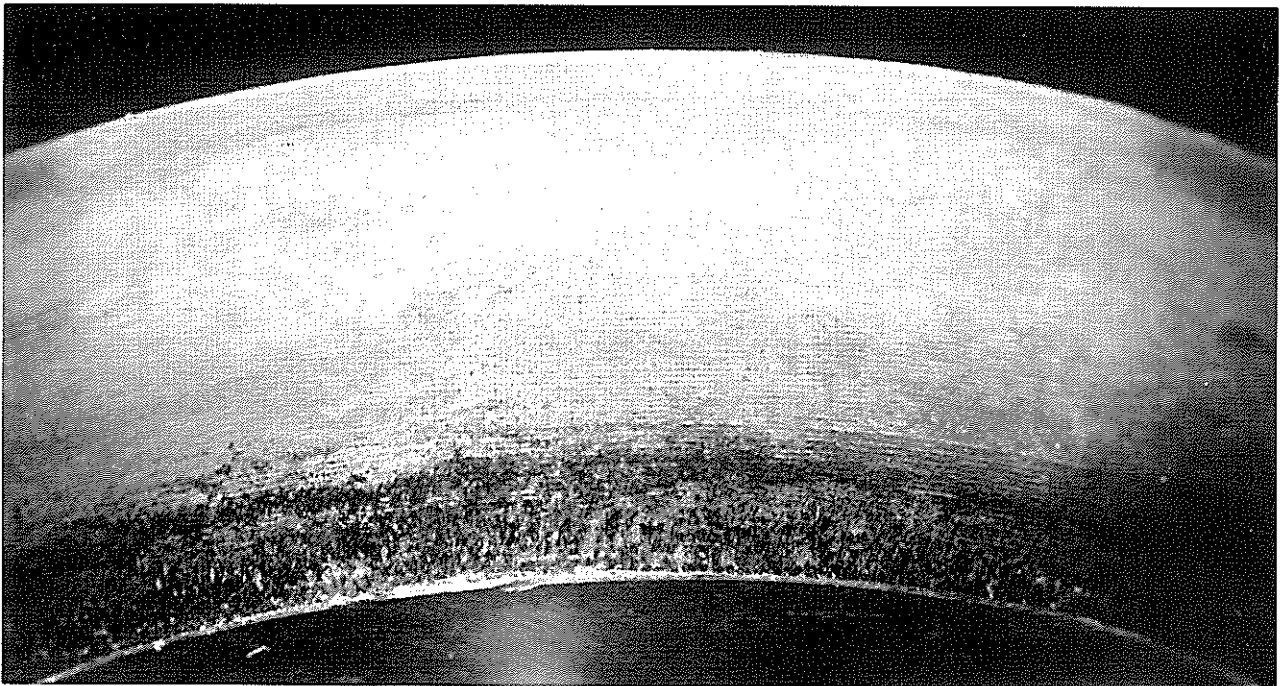


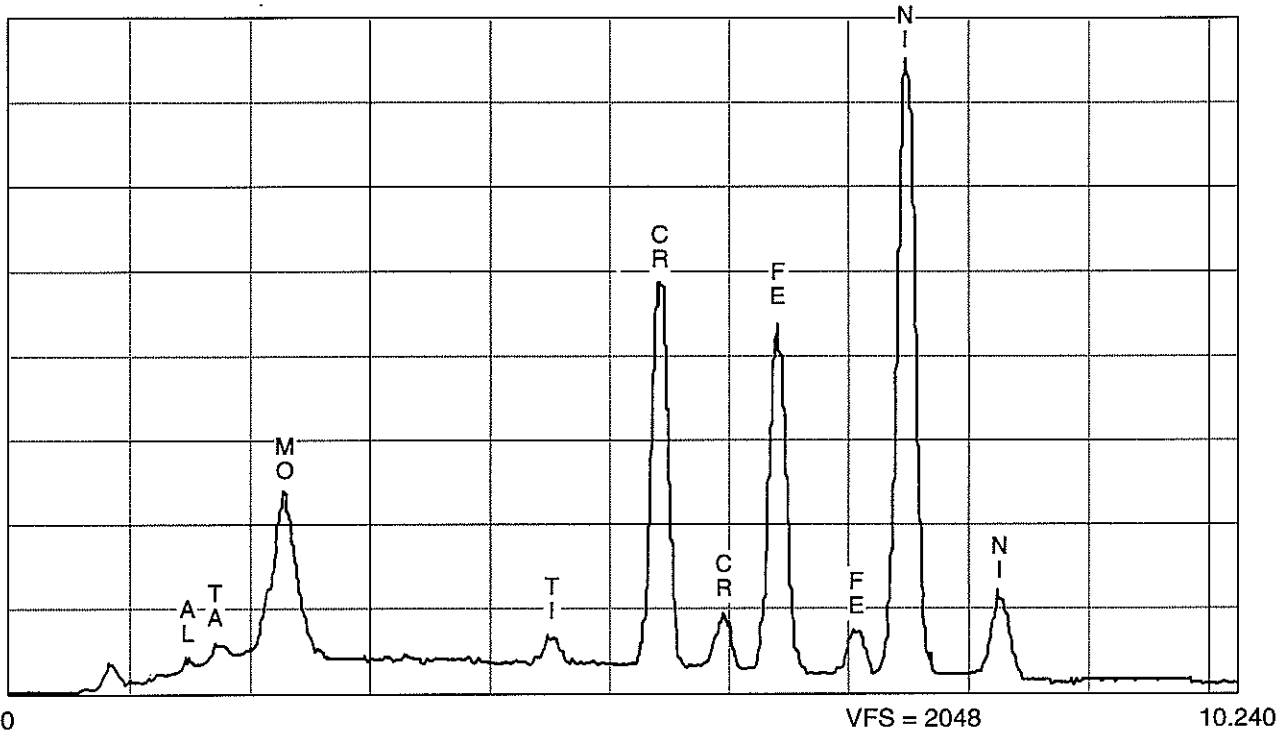
Fig. 37 Local fretting on the spherical rod end of the broken-open rod from the incident engine (NLR code S<sub>1</sub>)



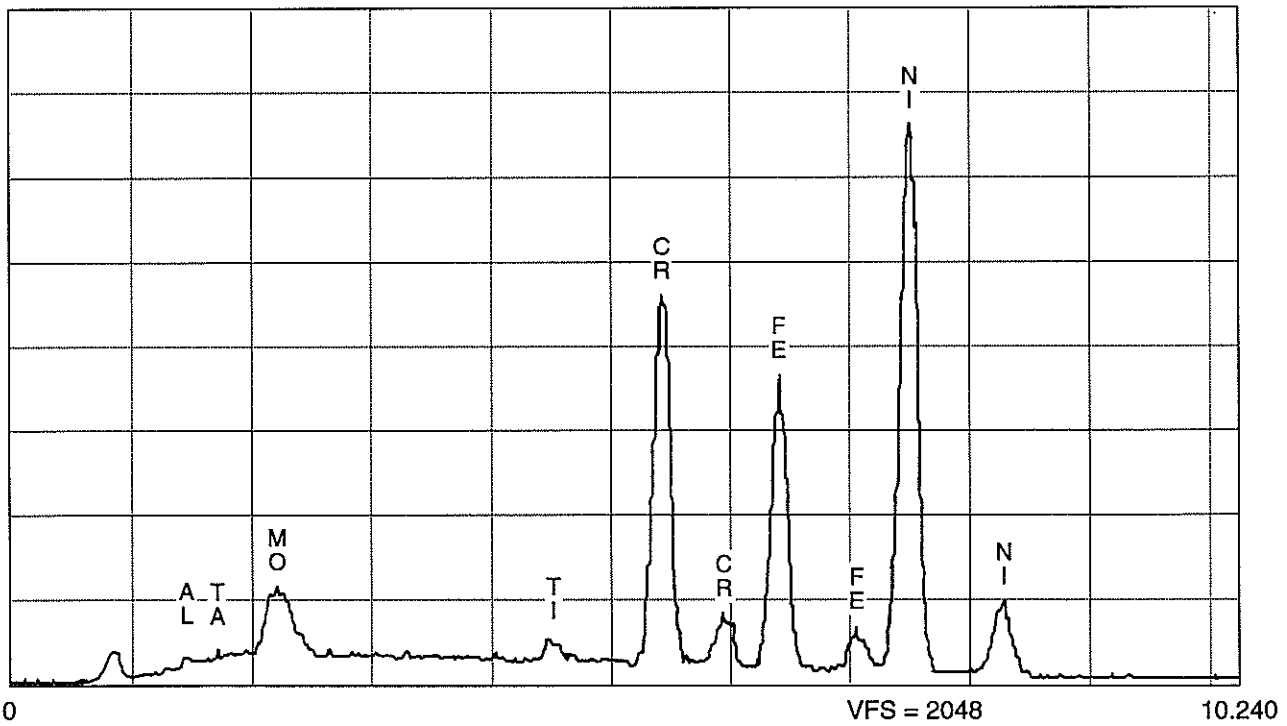
*Fig. 38 Local fretting on the spherical rod end of a broken-open rod (NLR code A)*



*Fig. 39 Local fretting on the spherical rod end of an uncracked rod (NLR code D)*

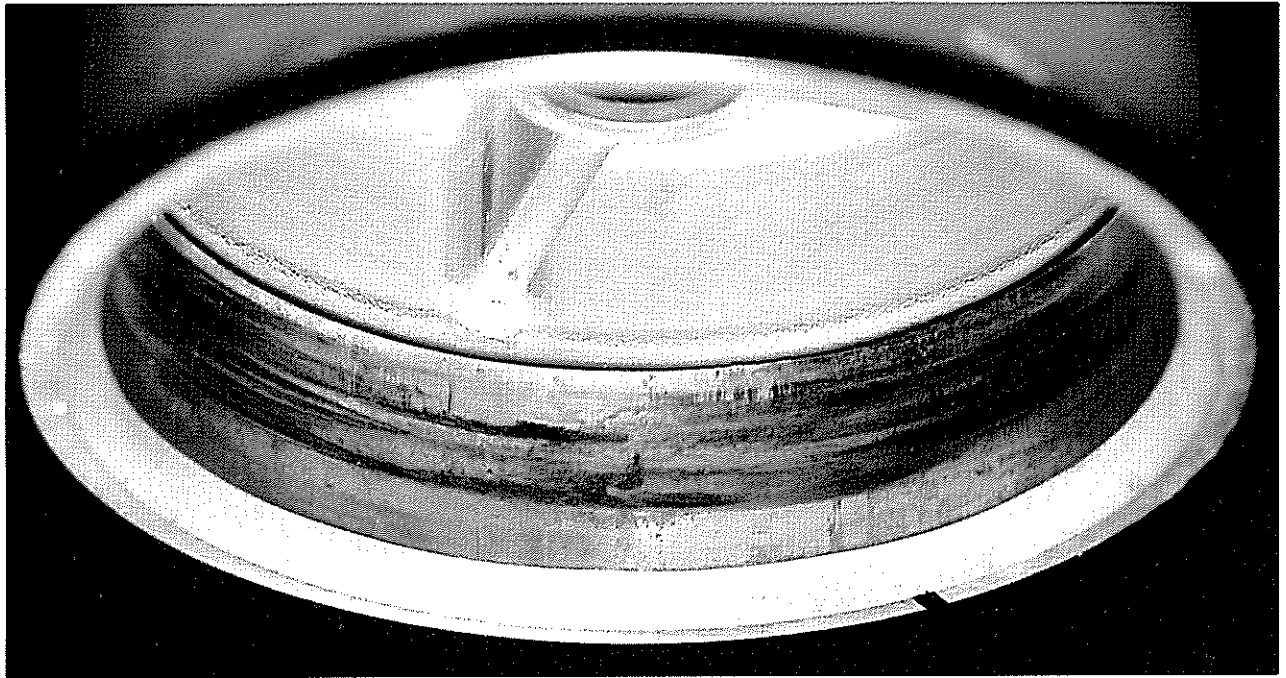


a) Spherical end of the broken rod



b) Surface of broken rod

Fig. 40 EDX surface analyses of the broken rod from the incident engine (NLR code S)



a) Diffuser casing side



b) Manifold side

*Fig. 41 Grooves on the inside ring surfaces of the air supply tube expansion sleeves from the 8 o'clock position on the incident engine*

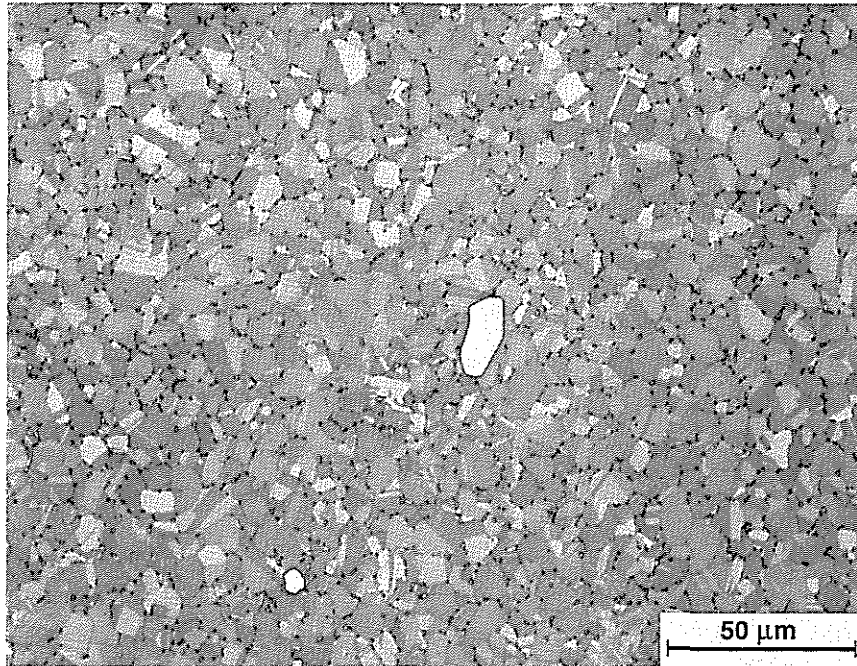


*Fig. 42 Microstructure of the broken rod (NLR code S) from the incident engine: ASTM grain size 11.6*

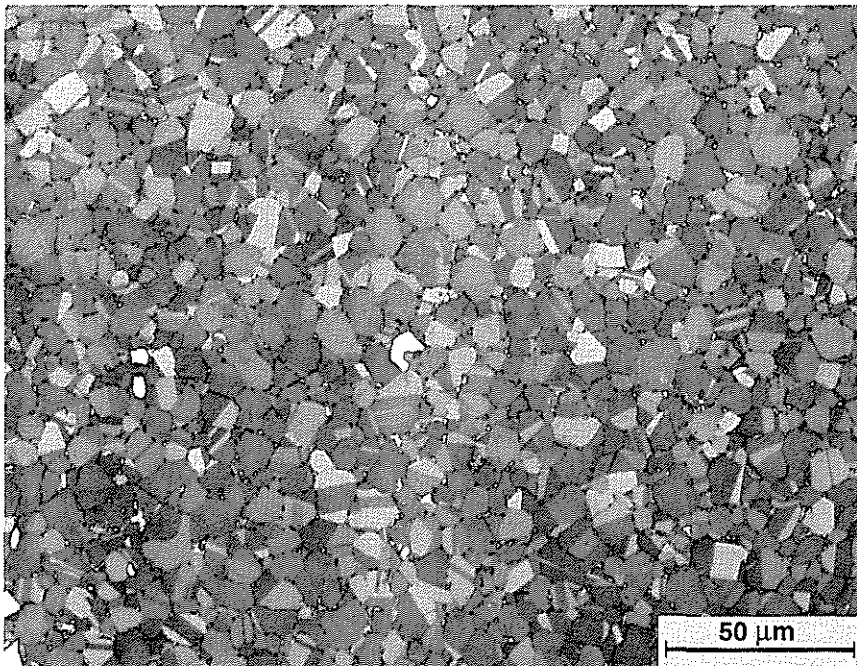


*Fig. 43 Microstructure of rod B (NLR code): ASTM grain size 11.2*

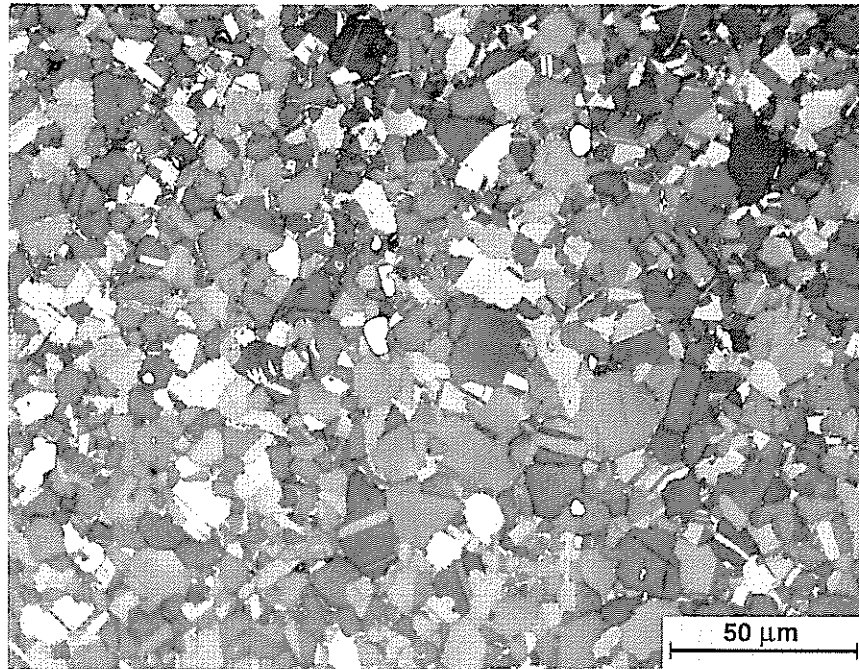


*Fig. 44 Microstructure of rod E (NLR code): ASTM grain size 10.5*

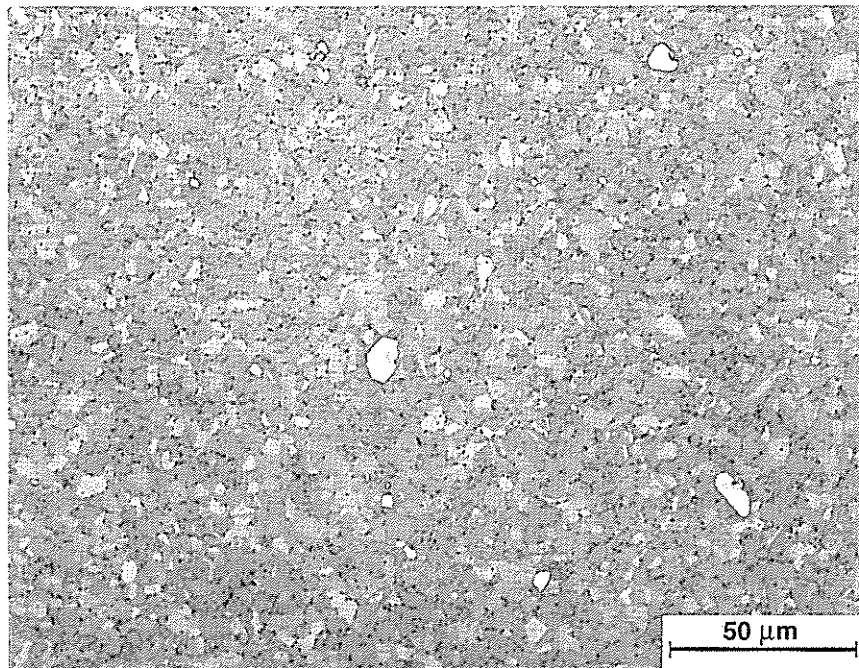


*Fig. 45 Microstructure of rod F (NLR code): ASTM grain size 12.8*

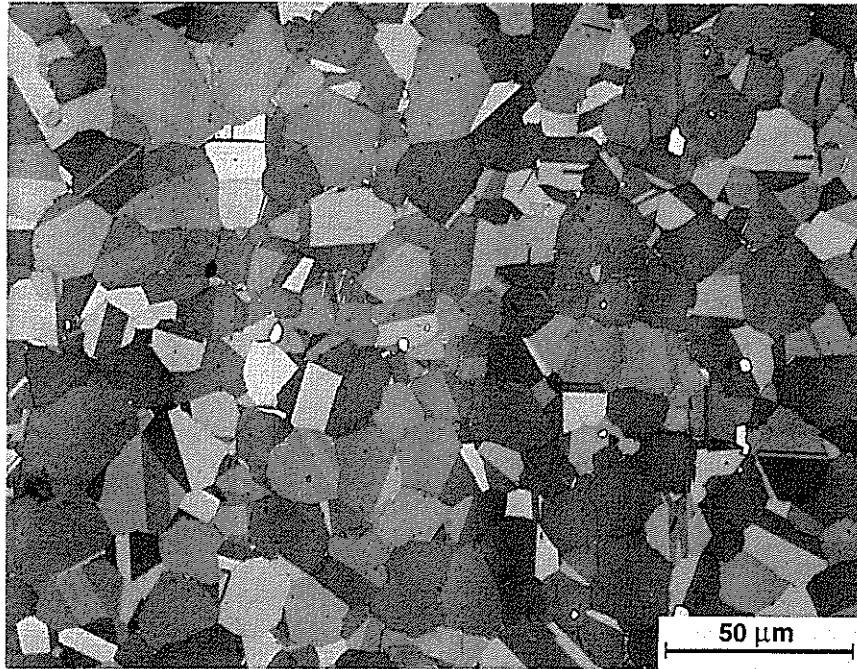


*Fig. 46 Microstructure of rod G (NLR code): ASTM grain size 9.5*





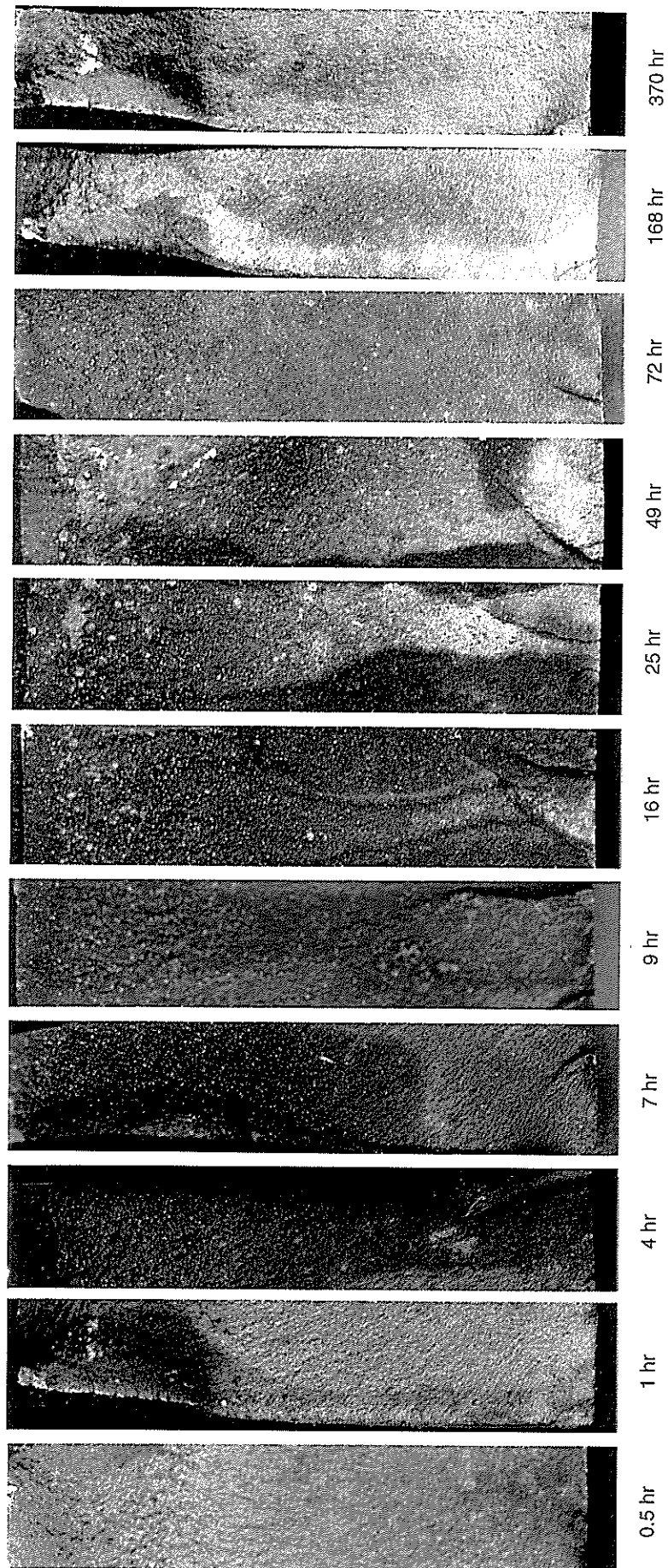


Fig. 48 Furnace oxidation of Inconel 718 Stage II fatigue fracture surfaces at 540° C - 550° C



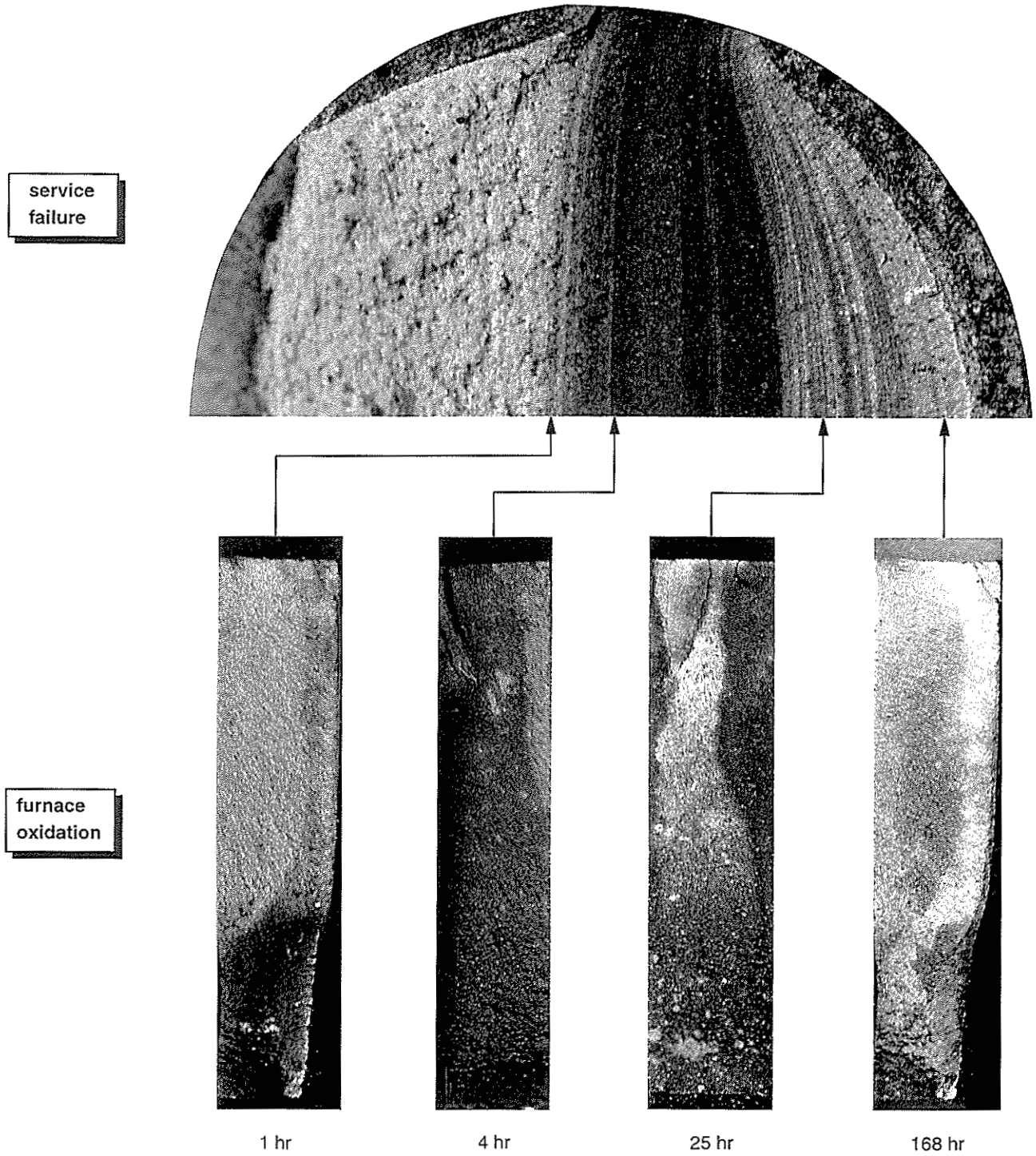
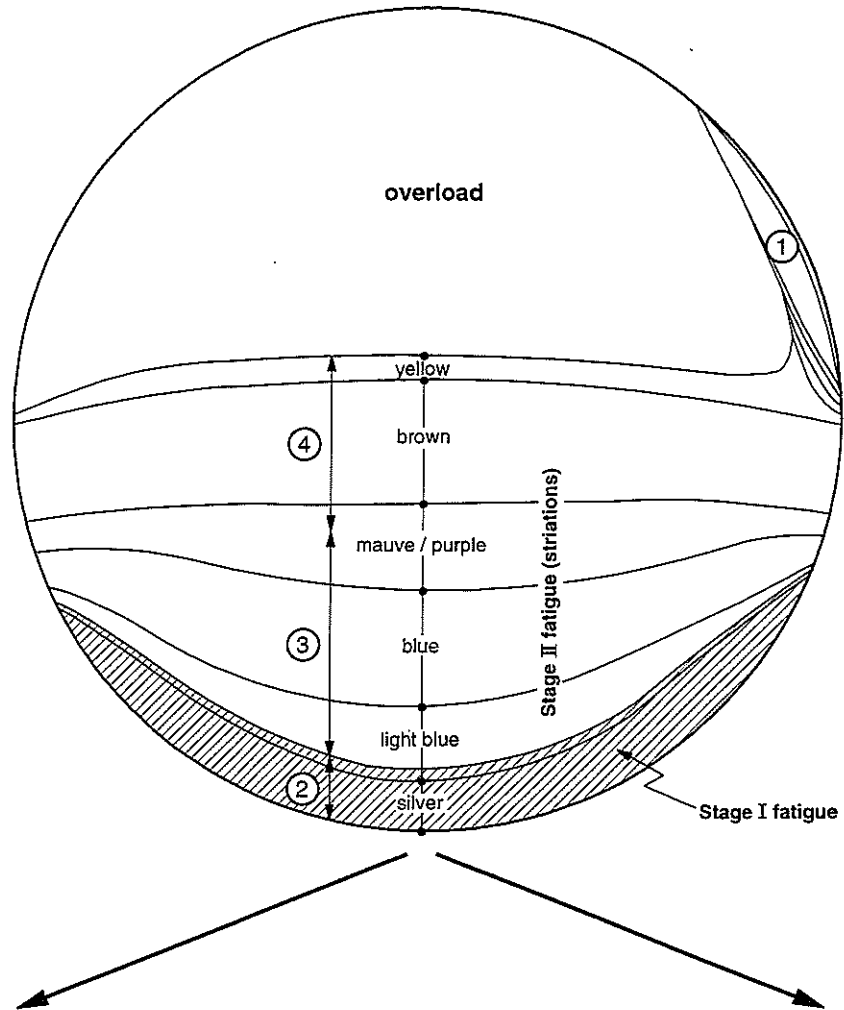


Fig. 49 A comparison of interference colours from furnace oxidation at  $540^{\circ}\text{C}$  -  $550^{\circ}\text{C}$  with the interference colours on the fracture surface of the broken rod end





Service History	Intervals			Fatigue fracture areas	
	EOT (hours)	LCF (cycles)	Flights	possibility A	possibility B
0 → 1st maintenance	410.9	2361	257	①	①
1st → 2nd maintenance	761.5	3082	326	② + ③	②
2nd maintenance → failure	143.5	343	57	④	③ + ④

BB85-35N

Fig. 50 Interpretation of the relation between fatigue fracture areas and engine operating history for the broken rod end